



Spectroscopic evaluation of several thulium doped laser materials via Fourier transform time-resolved spectroscopy  
by Richard Charles Martoglio

A thesis submitted in partial fulfillment of the requirements for the degree of Master of Science in Chemistry ( MONTANA STATE UNIVERSITY Bozeman, Montana August 1997  
Montana State University  
© Copyright by Richard Charles Martoglio (1997)

**Abstract:**

A new technique for the analysis of solid-state laser materials named Fourier Transform Time-Resolved Spectroscopy (FT-TRS) has been developed and implemented. FT-TRS has advantages over previous analysis techniques, primarily the time in which complete material characterization can be accomplished. The technique uses interferometric methods to collect sample emission after excitation over a broad spectral range while simultaneously characterizing the emission lifetime. In this way, analysis time is shortened considerably while providing information regarding absorption frequencies, emission frequencies and emission lifetimes which are essential for understanding the kinetics of the many photophysical processes which occur in these materials.

The interferometer used for our FT-TRS experiments can resolve spectral features to 0.25  $\text{cm}^{-1}$  over a range of nearly 23,000  $\text{cm}^{-1}$  (25,000-2,000  $\text{cm}^{-1}$ ). Temporal resolution to 20 nsec has been achieved. The implementation of an optically parametric oscillating laser enables material excitation from 23,000-5,500  $\text{cm}^{-1}$ .

FT-TRS has been used for the analysis of several different thulium ( $\text{Tm}^{3+}$ ) doped laser materials. The technique has proven to yield results consistent with earlier studies performed using different instrumentation. Emission rise and decay lifetimes for several electronic transitions have been determined. Mathematical fitting methods developed by Inokuti and Hirayama have proven to fit non-exponential emission decay that occurs in these materials. Subsequently, the kinetics which describe the many energy transfer events occurring after excitation have been investigated which has yielded the magnitudes of these radiative and non-radiative energy transfer processes.

**SPECTROSCOPIC EVALUATION OF SEVERAL THULIUM DOPED LASER  
MATERIALS VIA FOURIER TRANSFORM TIME-RESOLVED SPECTROSCOPY**

by

**Richard Charles Martoglio**

A thesis submitted in partial fulfillment  
of the requirements for the degree

of

**Master of Science**

in

**Chemistry**

**MONTANA STATE UNIVERSITY  
Bozeman, Montana**

**August 1997**

N378  
M3672

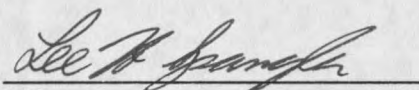
APPROVAL

of a thesis submitted by

Richard Charles Martoglio

This thesis has been read by each member of the thesis committee and has been found to be satisfactory regarding content, English usage, format, citations, bibliographic style, and consistency, and is ready for submission to the College of Graduate Studies.

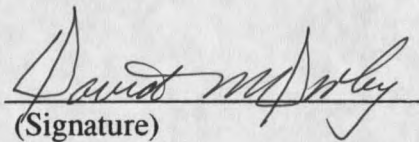
Dr. Lee Spangler

  
(Signature)

8/15/97  
Date

Approved for the Department of Chemistry

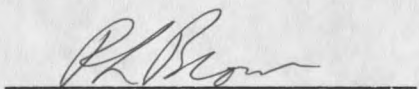
Dr. David Dooley

  
(Signature)

8/15/97  
Date

Approved for the College of Graduate Studies

Dr. Robert Brown

  
(Signature)

8/15/97  
Date

## STATEMENT OF PERMISSION TO USE

In presenting this thesis in partial fulfillment of the requirements for a master's degree at Montana State University-Bozeman, I agree that the Library shall make it available to borrowers under rules of the Library.

If I have indicated my intention to copyright this thesis by including a copyright notice page, copying is allowable only for scholarly purposes, consistent with "fair use" as prescribed in the U.S. Copyright Law. Requests for permission for extended quotation from or reproduction of this thesis in whole or in parts may be granted only by the copyright holder.

Signature Richard Charles Mayo

Date 8/15/97

## ACKNOWLEDGMENTS

I would like to thank Dr. Lee Spangler for his guidance, instruction, motivation and support while pursuing this degree. A very special thanks is extended to Dr. Ralph Hutcheson, Dr. Randy Equall and everyone at Scientific Materials Corporation for their provision of sample laser materials and invaluable knowledge. I would also like to express thanks to the people who helped get this project started through the loaning of knowledge and equipment, namely, Dr. Patrik Callis and the Callis group, Dr. John Carlsten and the Carlsten group, Dr. Rufus Cone and the Cone group, Mr. Lee David, Mr. Dallas Johnston, Dr. Berk Knighton, Mr. Ray Larsen, Dr. Brian Metzger and Dr. David Singel and the Singel group. This project is completely a group effort and, therefore, I would like to thank my labmates Mr. Bruce Farris, Mr. Richard Hanson, Ms. Amy Hyfield, Mr. Anthony Smith and Ms. Wendi Sonnenberg. Without their efforts and perseverance success of this project could not be realized. And a final thanks goes to my parents for their caring and continual support.

## TABLE OF CONTENTS

	Page
1. INTRODUCTION .....	1
General .....	1
Statement of the Problem .....	2
Spectroscopy of Rare-Earth Crystalline Laser Materials .....	3
The Chemistry and Physics of Laser Materials .....	4
Stark Level Employment in Operating Schemes .....	6
Dopant Ion Concentrations .....	7
Temperature Effects .....	8
Thulium Doped Materials .....	9
Co-Doped Materials .....	11
2. TIME-RESOLVED FOURIER TRANSFORM SPECTROSCOPY .....	15
Background .....	15
Step-Scan FTS Technique .....	16
Normalization of FT-TRS and Inherent Spectral Noise .....	20
TRSNomenclature .....	23
3. EXPERIMENTAL PROCEDURE .....	26
Sample Laser Materials .....	26
Experimental Apparatus .....	27
The Material Characterization Process .....	34
4. EXPERIMENTAL RESULTS .....	36
Absorption Spectra .....	36
Continuous Fluorescence Spectra .....	43
Time-Resolved Spectra .....	50
Excitation Via the $^3H_4$ Manifold .....	50
Tm <sup>3+</sup> :YAG .....	50
Tm <sup>3+</sup> :YALO .....	56
Tm <sup>3+</sup> :YSO .....	59
Tm <sup>3+</sup> :YO .....	62
Tm <sup>3+</sup> :LAG .....	63

TABLE OF CONTENTS - Continued

	Page
Excitation Via the $^1G_4$ Manifold .....	63
$Tm^{3+}$ :YAG.....	63
$Tm^{3+}$ :YALO.....	66
Excitation Via the $^1D_2$ Manifold .....	67
$Tm^{3+}$ :YAG.....	69
$Tm^{3+}$ :YALO.....	70
 5. DISCUSSION OF RESULTS .....	 75
General Experimental Results .....	75
$Tm^{3+}$ :YAG.....	75
$Tm^{3+}$ :YALO.....	77
Generation and Fitting of Experimental Decay Curves .....	78
Generation of Decay Curves .....	78
Mathematical Fits of Experimental Decay Curves .....	79
Kinetic Model of Experimental Data .....	85
Derivation of Rate Equations .....	85
Low Concentration $Tm^{3+}$ :YAG.....	86
High Concentration $Tm^{3+}$ :YAG .....	87
 6. CONCLUSIONS & SUMMARY .....	 93
Advantages and Limitations of FT-TRS .....	93
Closing Remarks.....	97
 REFERENCES CITED .....	 100

## LIST OF TABLES

Table	Page
1. Experimental Lifetimes of Transitions in $Tm^{3+}$ Doped Materials .....	72
2. $^3F_4$ Manifold Population (Rise) Times for $Tm^{3+}$ Doped Materials .....	74
3. Values for Ionic Separation and $C/C_0$ Derived from the IH Fit .....	84
4. Summary of Terms Used for the Kinetic Model .....	89

## LIST OF FIGURES

Figure	Page
1. The YAG crystal lattice .....	5
2. $2\mu\text{m}$ lasing operation scheme for $\text{Tm}^{3+}:\text{YAG}$ .....	10
3. IR lasing operation scheme for $\text{CTH}:\text{YAG}$ .....	12
4. Formation of the interferogram in rapid-scan mode vs. step-scan mode .....	18
5. Derivation of the time-resolved spectrum .....	19
6. Generation of systematic noise in FT-TRS spectra .....	21
7. Interferograms and corresponding spectra .....	22
8. A step-scan emission spectrum .....	24
9. Apparatus employed for absorption and emission studies .....	28
10. The Bruker IFS 66 step-scan interferometer .....	29
11. Spectra for detector/beamsplitter combinations .....	30
12. Spectra for KG3 and RG715 optical filters .....	33
13. IR (top) and visible absorption spectra for $\text{Tm}^{3+}:\text{YAG}$ .....	38
14. IR (top) and visible absorption spectra for $\text{Tm}^{3+}:\text{LAG}$ .....	39
15. IR (top) and visible absorption spectra for $\text{Tm}^{3+}:\text{YALO}$ .....	40
16. IR (top) and visible absorption spectra for $\text{Tm}^{3+}:\text{YSO}$ .....	41
17. IR (top) and visible absorption spectra for $\text{Tm}^{3+}:\text{YO}$ .....	42

LIST OF FIGURES - Continued

	Page
18. IR (top) and visible continuous emission spectra for $\text{Tm}^{3+}:\text{YAG}$ .....	45
19. IR (top) and visible continuous emission spectra for $\text{Tm}^{3+}:\text{LAG}$ .....	46
20. IR (top) and visible continuous emission spectra for $\text{Tm}^{3+}:\text{YALO}$ .....	47
21. IR (top) and visible continuous emission spectra for $\text{Tm}^{3+}:\text{YSO}$ .....	48
22. IR (top) and visible continuous emission spectra for $\text{Tm}^{3+}:\text{YO}$ .....	49
23. Time-resolved IR fluorescence spectrum for 0.25% $\text{Tm}^{3+}:\text{YAG}$ . 400 $\mu\text{sec}$ time resolution, 200 time slices, 10 co-adds .....	51
24. Decay of the ${}^3\text{F}_4 \rightarrow {}^3\text{H}_6$ transition for the 0.25% $\text{Tm}^{3+}:\text{YAG}$ sample .....	52
25. Time-resolved IR fluorescence spectrum for 0.25% $\text{Tm}^{3+}:\text{YAG}$ . 20 $\mu\text{sec}$ time resolution, 200 time slices and 20 co-adds .....	53
26. Decay of the ${}^3\text{H}_4 \rightarrow {}^3\text{F}_4$ transition at $6,800 \text{ cm}^{-1}$ for the 5 $\text{Tm}^{3+}:\text{YAG}$ samples.....	54
27. Log of intensity vs. time for the decay of ${}^3\text{H}_4 \rightarrow {}^3\text{F}_4$ transition at $6,800 \text{ cm}^{-1}$ for the 5 $\text{Tm}^{3+}:\text{YAG}$ samples .....	55
28. Population of the ${}^3\text{F}_4 \rightarrow {}^3\text{H}_6$ fundamental IR transition for the 5 $\text{Tm}^{3+}:\text{YAG}$ samples.....	56
29. Population of the ${}^3\text{H}_4 \rightarrow {}^3\text{F}_4$ transition at $6,800 \text{ cm}^{-1}$ for 0.25% $\text{Tm}^{3+}:\text{YAG}$ .....	57
30. Time-resolved fluorescence spectrum for 0.1% $\text{Tm}^{3+}:\text{YALO}$ . 250 $\mu\text{sec}$ time resolution, 200 time slices, 10 co-adds .....	58
31. Decay of the ${}^3\text{F}_4 \rightarrow {}^3\text{H}_6$ transition for 0.1% $\text{Tm}^{3+}:\text{YALO}$ .....	58
32. Log of intensity vs. time for the decay of the ${}^3\text{H}_4 \rightarrow {}^3\text{F}_4$ transition at $6,800 \text{ cm}^{-1}$ for the 2 $\text{Tm}^{3+}:\text{YALO}$ samples .....	59

LIST OF FIGURES - Continued

	Page
33. Population of the ${}^3F_4 \rightarrow {}^3H_6$ fundamental IR transition for the 2 $Tm^{3+}$ :YALOsamples.....	60
34. Decay of the ${}^3F_4 \rightarrow {}^3H_6$ fundamental transition for $Tm^{3+}$ :YSO .....	61
35. Log of intensity versus time for the decay of the ${}^3H_4 \rightarrow {}^3F_4$ transition at $6,800\text{ cm}^{-1}$ for $Tm^{3+}$ :YSO .....	61
36. Decay of the ${}^3F_4 \rightarrow {}^3H_6$ fundamental transition for $Tm^{3+}$ :YO .....	62
37. Log of intensity versus time for the decay of the ${}^3H_4 \rightarrow {}^3F_4$ transition at $6,500\text{ cm}^{-1}$ for $Tm^{3+}$ :YO .....	63
38. Extracts at $20\ \mu\text{sec}$ after red (upper) and blue excitation for $0.25\% Tm^{3+}$ :YAG.....	65
39. Trace integrations after blue excitation for $0.1\% Tm^{3+}$ :YALO .....	67
40. FT-TRS spectrum for $0.1\% Tm^{3+}$ :YALO for the $13,000\text{ cm}^{-1}$ region .....	68
41. Time-resolved visible (blue) fluorescence spectrum for $0.25\%$ $Tm^{3+}$ :YAG. $5\ \mu\text{sec}$ time resolution, 40 time slices and 20 co-adds .....	69
42. Log of intensity versus time for the decay of the ${}^1G_4 \rightarrow {}^3H_6$ transition at $22,000\text{ cm}^{-1}$ for the 3 $Tm^{3+}$ :YAG samples studied .....	70
43. Time-resolved visible (red) fluorescence spectrum for $0.25\%$ $Tm^{3+}$ :YAG.....	71
44. Integration method employed to generate experimental trace decaycurves.....	79
45. IH (solid line) fit to the ${}^3H_4 \rightarrow {}^3F_4$ non-exponential decay for $2.4\% Tm^{3+}$ :YAG.....	81
46. IH (solid line) fit to the ${}^3H_4 \rightarrow {}^3F_4$ non-exponential decay for $4.0\% Tm^{3+}$ :YAG.....	82

LIST OF FIGURES - Continued

	Page
47. IH (solid line) fit to the ${}^3\text{H}_4 \rightarrow {}^3\text{F}_4$ non-exponential decay for 5.2% $\text{Tm}^{3+}:\text{YAG}$ .....	82
48. Ionic separation ( $\text{\AA}$ ) versus $C/C_0$ derived from the IH fit .....	84
49. Energy level diagram for $\text{Tm}^{3+}:\text{YAG}$ .....	86
50. Modeled decay (dashed) from manifold 3 ( ${}^3\text{H}_4$ ) vs. 0.25% experimental decay .....	88
51. Modeled decay (dashed) from manifold 1 ( ${}^3\text{F}_4$ ) vs. 0.25% experimental decay .....	88
52. Modeled decay (dashed) from manifold 3 ( ${}^3\text{H}_4$ ) vs. 2.4% experimental decay .....	90
53. Modeled decay (dashed) from manifold 3 ( ${}^3\text{H}_4$ ) vs. 4.0% experimental decay .....	91
54. Modeled decay (dashed) from manifold 3 ( ${}^3\text{H}_4$ ) vs. 5.2% experimental decay .....	91
55. Population of the $\text{Tm}^{3+} {}^3\text{H}_4$ (open circles) and $\text{Ho}^{3+} {}^5\text{I}_7$ manifolds after $12,800 \text{ cm}^{-1}$ excitation .....	94
56. FT-TRS spectrum for the population of the ${}^3\text{F}_4$ and ${}^5\text{I}_7$ manifolds of $\text{Tm}^{3+}$ and $\text{Ho}^{3+}$ , respectively in $\text{CTH}:\text{YAG}$ .....	95

## ABSTRACT

A new technique for the analysis of solid-state laser materials named Fourier Transform Time-Resolved Spectroscopy (FT-TRS) has been developed and implemented. FT-TRS has advantages over previous analysis techniques, primarily the time in which complete material characterization can be accomplished. The technique uses interferometric methods to collect sample emission after excitation over a broad spectral range while simultaneously characterizing the emission lifetime. In this way, analysis time is shortened considerably while providing information regarding absorption frequencies, emission frequencies and emission lifetimes which are essential for understanding the kinetics of the many photophysical processes which occur in these materials.

The interferometer used for our FT-TRS experiments can resolve spectral features to  $0.25 \text{ cm}^{-1}$  over a range of nearly  $23,000 \text{ cm}^{-1}$  ( $25,000\text{-}2,000 \text{ cm}^{-1}$ ). Temporal resolution to 20 nsec has been achieved. The implementation of an optically parametric oscillating laser enables material excitation from  $23,000\text{-}5,500 \text{ cm}^{-1}$ .

FT-TRS has been used for the analysis of several different thulium ( $\text{Tm}^{3+}$ ) doped laser materials. The technique has proven to yield results consistent with earlier studies performed using different instrumentation. Emission rise and decay lifetimes for several electronic transitions have been determined. Mathematical fitting methods developed by Inokuti and Hirayama have proven to fit non-exponential emission decay that occurs in these materials. Subsequently, the kinetics which describe the many energy transfer events occurring after excitation have been investigated which has yielded the magnitudes of these radiative and non-radiative energy transfer processes.

## CHAPTER 1

### INTRODUCTION

#### General

Laser based analysis systems have been implemented in many areas of scientific research, as well as in monitoring applications and medicine. Examples include the study and identification of environmental pollutants through remote sensing (LIDAR), the determination of molecular orientation at a surface (SERS), the process of soft-ionization in laser desorption mass spectrometry (MALDI) and the development of surgical lasers. The creation of new laser technology and the improvement of laser designs currently in use is of paramount significance when considering the increasing complexity and importance of their roles in real world applications. As more demands are being made upon the scientific community to improve laser performance advances are also required in the analysis of the materials that serve as the lasing media.

Solid-state lasers are proving to be a practical source of light emission in the aforementioned areas of research. These lasers are very durable, are usually compact in size, quite powerful and generally can be operated at a variety of repetition rates. Coherent photon output in solid-state systems is dependent on the crystalline lasing

medium implemented. Laser performance is directly dependent on the optical properties of the lasing medium, such as emission. Spectroscopic analysis methods allow for a better understanding of the physical processes which occur in these crystalline materials. Based on the studies of these processes, materials may be evaluated and possibly improved.

### Statement of the Problem

Currently, there are several hundred crystalline materials that have the potential for use in solid-state lasers. New materials may be developed at rapid rates, with crystal growth times generally on the order of a few days up to two weeks. Additionally, many growers have the capability of creating a variety of finished products in a single growing period. For example, Scientific Materials Corporation of Bozeman, MT created nearly fifty different materials in a two month span. Due to this ability to quickly manufacture materials and the limitations of current material analysis techniques it is the goal of this research to develop and apply a spectroscopic method that allows for rapid and accurate material characterization. Upon characterization, information may then be fed back to the grower to aid in their engineering processes or determine if the material is suitable for use in an operating laser system.

The method employed will allow for developing a better understanding of energy transfer processes which occur (radiative and nonradiative) after excitation. Spectroscopic results obtained via the new method will be compared to known and accepted data for validation of the method. In addition, a working kinetic model based

upon experimental results will be generated. During the initial studies of this project we hope to exploit the advantages of the technique while uncovering problems and limitations.

### Spectroscopy of Rare-Earth Crystalline Laser Materials

The spectroscopic parameters of laser materials have been studied for over 30 years. Johnson, *et al.* in 1965 and 1966 studied emission from several different rare-earth ions doped into yttrium aluminum garnet ( $Y_3Al_5O_{12}$  or YAG)(1).

Solid-state laser materials tend to have many absorption bands which are made up of relatively narrow line features. The materials absorb light over a broad wavelength region, but do so selectively due to the narrow line widths. In order to fully characterize a material it is beneficial to selectively excite the sample at many different energies and often at different sites within a particular absorption manifold. Upon excitation the material may then emit light. The emission is typically narrow band, but can occur over a broad wavelength region. Most spectroscopic emission data has been obtained by using either a laser or conventional source such as a tungsten or mercury lamp to excite the material. Emitting wavelengths from the material are typically dispersed using a monochromator and impinged on a photo-sensitive detector responsive to the wavelength(s) of interest. Emission lifetimes may be measured after pulsed excitation with the addition of an oscilloscope or a boxcar with sufficient temporal resolution capabilities. The determination of the emission lifetimes with a high degree of accuracy and precision is necessary to determine energy transfer rates. This method of analysis

is a very reliable and proven one, but is quite tedious and time-consuming.

The above characteristics of these materials shed light upon the requirements needed to effectively perform spectroscopic analyses. It is imperative that a narrow band source be employed that is tunable over a large frequency range (ultra-violet to near-infrared) to fully exploit the absorption features of the material. Recent laser developments (Optical Parametric Oscillation, OPO) have made this possible. Also, because many emissions occur within a nanosecond time frame, short output pulses are required. Since emission lifetimes can vary significantly for different processes (from milliseconds for emission from the first excited state to nanoseconds for inter-manifold transitions), variation of the laser output repetition rate is essential to allow for complete relaxation between pulses.

The device employed to detect and analyze emitting radiation must operate over a wide spectral range with sufficient resolution capabilities. In order to analyze data rapidly the system must simultaneously pass, detect and resolve as many emitting wavelengths as possible and the system must resolve the emission in 3 dimensions: intensity, wavelength and time. This is the major time limiting factor of previous analysis designs. We have found that the solution to the above requirements is the technique of step-scan interferometry and is outlined in Chapter 2.

### The Chemistry and Physics of Laser Materials

The materials used in this study were grown by the Czochralski technique. The materials are conceived by starting with the compounds that will form the crystalline

lattice. It is imperative that these compounds be free of dopant or impurity ions, such as  $\text{Nd}^{3+}$  and  $\text{OH}^-$ , respectively. Typically, an iridium crucible is used to contain the "melt" which consists of the lattice precursors. The growing process is carried out at temperatures above 2200 degrees celcius. The dopant ion is introduced into the melt when it reaches the correct temperature for material formation. The crystal is then pulled slowly from the melt, for example, 0.6 mm/hr during Nd:YAG crystal formation(2). The temperature of the melt must be rigorously controlled by the grower to ensure that the dopant ion is distributed properly throughout the crystal as it is pulled. The dopant ion replaces a matrix ion (yttrium) at certain sites in YAG (see Figure 1), for example, which leads to a material that is capable of producing radiative emission that

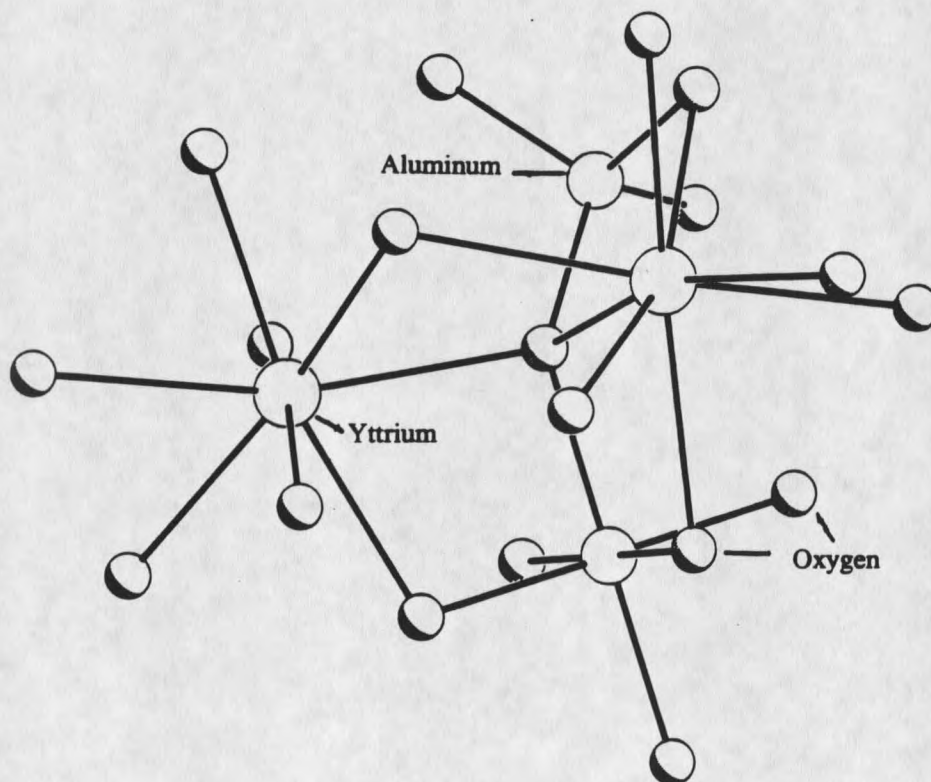


Figure 1. The YAG crystal lattice.

may be used for lasing under proper conditions(3). Again, it is important that the matrix and dopant materials be free of outside impurities such as the hydroxide ion. Hydroxide ion impurities with magnitudes of 1 to 4% in  $\text{Nd}^{3+}:\text{YAG}$  have shown to cause a decrease of approximately 50% in lasing output power(4). This decrease is believed to be due to direct interaction of the  $\text{Nd}^{3+}$  ion with the  $\text{OH}^-$  impurity that resides in the dodecahedral site of the YAG lattice.

#### Stark Level Employment In Operating Schemes

It has been stated that the initial action to be taken when performing spectroscopic analyses of solid-state laser media is the identification and location of the characteristic absorption bands (Stark manifolds) and their corresponding features (Stark levels)(3). This process is most easily accomplished by light absorption methods. This determination allows for selective excitation, experimental emission energy transfer assignments and determination of other energy transfer processes such as upconversion and cross-relaxation, for example. While pre-existing calculated and experimental absorption data is a valuable resource, it is important to perform absorption measurements when samples are obtained for study, due to the possibility of changes in the optical properties caused by impurities.

Stark manifold location and level structure is governed by the electrostatic interaction of the 4f electrons with one another, the spin-orbit coupling of the electrons and the influence of the lattice crystal field.(5) The Coulombic interaction generates the  $2s+1L$  terms which are generally separated by thousands of  $\text{cm}^{-1}$ . The spin-orbit coupling splits the total angular momentum J states. The influence of the crystal field

then splits the Stark manifolds into their fine structure (Stark levels) with a degeneracy equal to  $2J+1$ (5). The strength of the crystal field interaction with the dopant ion determines the energy spacing of the Stark levels within a given manifold. Most often, materials grown using rare-earth metals with a +3 charge experience a weak interaction with the crystal field due to the inner 4f electrons being shielded from the surrounding environment (host lattice) by the outer 5s and 5p electrons.(3,5,6) Consequently, the energy spacing between Stark levels is small, typically on the order of  $10-100 \text{ cm}^{-1}$ . Often, many different lattice materials are grown with the same dopant ion. This is done so that small energy shifts of the Stark levels may be accomplished leading to a laser material that may be employed in a desired application.

The crystal field is also responsible for inducing oscillator strength into specific transitions. The magnitude of the oscillator strength reveals the probability of radiative energy transfer between given Stark levels.

#### Dopant Ion Concentrations

Spectroscopic analysis of emission from the material as dopant concentration is varied over a large gradient is required in order to investigate ion-ion interactions(3). An experiment performed by Zhekov, *et al.*(7), described the effects of varying the concentration of  $\text{Er}^{3+}$  ions doped into YAG. The authors found that the optimum amount of doped  $\text{Er}^{3+}$  was 15% when observing the IR fluorescence decay at approximately  $6,000 \text{ cm}^{-1}$ . At very low (0.5%) and very high (100%) amounts of  $\text{Er}^{3+}$  the experimental lifetime decreased dramatically from a maximum lifetime of 9 msec obtained at 6%  $\text{Er}^{3+}$  to 6.5 msec and 0.25 msec, respectively. These results were

confirmed by Shi, *et al.*(8) in a similar study. Similarly, Becker, *et al.*(9), as well as Armagan, *et al.*(10) showed that as the  $\text{Tm}^{3+}$  concentration in YAG was increased the lifetime of the experimental emission from the  $^3\text{H}_4$  manifold near 780 nm to the  $^3\text{H}_6$  ground state became significantly shorter.

When high dopant ion concentrations are used self-quenching becomes an issue of concern. Self-quenching, often called concentration quenching or cross-relaxation, is a non-radiative, resonant energy transfer that can depopulate the upper laser level and have a detrimental effect on the lasing process as in the case of  $\text{Er}^{3+}:\text{YAG}$ .(7,8) Self-quenching is due solely to dopant ion-dopant ion interactions. As the concentration of the dopant ion increases the ions become closer to each other spatially. It has been determined by Dexter, *et al.*(11), as well as, Inotaki and Hirayama(12), that this cross-relaxing quenching process is generally dominated by electric dipole-dipole interactions described by an  $R^{-6}$  distance dependence. The process may also be dependent on the energy of the exciting photons(8), as well as the temperature of the crystal.

### Temperature Effects

Radiative and non-radiative emission lifetimes in  $\text{Tm}^{3+}$  doped laser materials are substantially affected by changes in temperature. Zverev, *et al.*(13), observed that for  $\text{Tm}^{3+}:\text{YAG}$  as temperature was increased from 77 to 900 degrees K the experimental emission lifetime of the  $^3\text{F}_4 \rightarrow ^3\text{H}_6$  transition decreased from 8.5ms to 2.5ms. This effect was described as temperature quenching. The decrease in lifetime is due to an increase in the probability of stimulated nonradiative (vibronic) transitions that depopulate the upper-laser manifold of the material ( $^3\text{F}_4$ )(14). In effect, as temperature increases, the

non-radiative processes (phonons, eg.) that occur within a sample begin to dominate the radiative processes. It is known that non-radiative decay events, as well as their reliance on variance in temperature are determined by the size of the dopant ion and its symmetry within a lattice(15). Therefore, for  $Tm^{3+}$  doped into different lattices, lifetimes may decrease over a temperature gradient with varying degrees of magnitude. It should be noted that a decrease in fundamental lifetime did not occur until the temperature reached approximately 475 K. A similar trend has been observed for lasing output power in three  $Tm^{3+}$  doped materials. As the crystal temperature was raised from 258 to 303 K the output power in Tm:YAG, Tm:YLAG and Tm:LAG decreased 8%, 7% and 11%, respectively(16).

Based on theoretical calculations, Riseberg and Weber(5) have shown that as temperature is increased from 0 to 400 degrees K, the rate of non-radiative multiphonon emission increases substantially and varies depending on the number of phonons involved in the emission. This supports the theory that as temperature is increased non-radiative decay becomes very significant and can have a detrimental effect on radiative energy transfer.

### Thulium

$Tm^{3+}$  has been used as an activator ion in laser materials for approximately 30 years(1,2) and is the main ion of focus in our studies.  $Tm^{3+}$  follows a quasi-four-level laser operating scheme with one metastable state when introduced as the dopant ion in YAG, where one  $Y^{3+}$  ion is replaced by one  $Tm^{3+}$  ion(3,17).

Most often, the  ${}^3\text{H}_4$  Stark manifold near  $12,800\text{ cm}^{-1}$  is pumped to initiate the energy transfer process where simultaneous radiative and non-radiative emissions occur from the  ${}^3\text{H}_4$  manifold to the  ${}^3\text{H}_5$  manifold. At sufficiently large  $\text{Tm}^{3+}$  concentrations, non-radiative energy decay to the  ${}^3\text{F}_4$  manifold readily occurs(18). Non-radiative multiphonon emission dominates the energy decay from the  ${}^3\text{H}_5$  to the  ${}^3\text{F}_4$  manifold because of the small energy gap ( $2,000\text{ cm}^{-1}$ ). This is followed by a long-lived radiatively dominated emission to the  ${}^3\text{H}_6$  ground state (see Figure 2). These emission

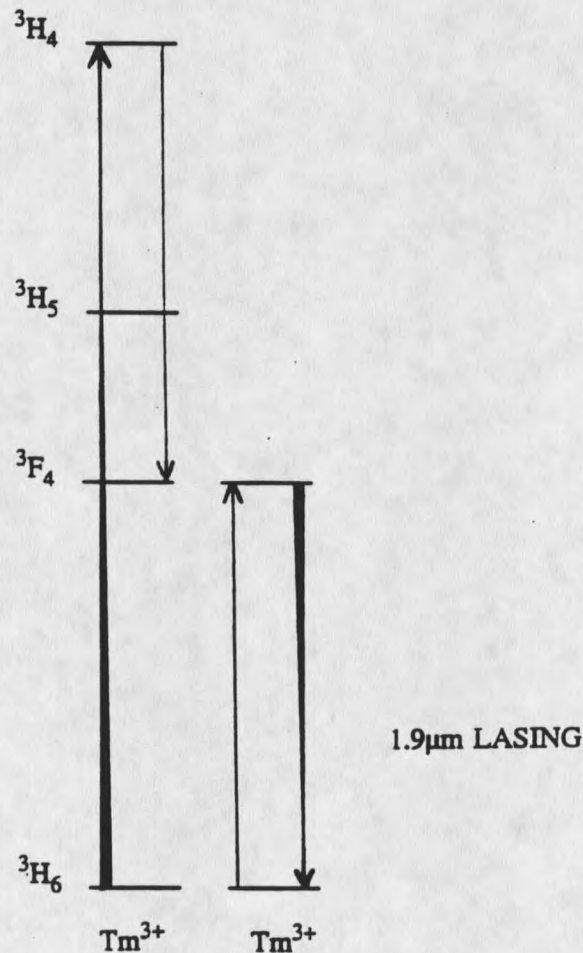


Figure 2.  $2\mu\text{m}$  lasing operation scheme for  $\text{Tm}^{3+}:\text{YAG}$ .

processes have been studied previously(1,9,18,20,21).

An additional and very important photophysical process that occurs in  $\text{Tm}^{3+}:\text{YAG}$  is also shown in Figure 2. This is the cross-relaxation process which occurs due to the resonance caused by the energy gap between the  ${}^3\text{F}_4\text{-}{}^3\text{H}_4$  and  ${}^3\text{F}_4\text{-}{}^3\text{H}_6$  manifolds. At large enough dopant-ion concentrations the emission from the  ${}^3\text{H}_4$  to the  ${}^3\text{F}_4$  manifold of one  $\text{Tm}^{3+}$  is quenched by a neighboring  $\text{Tm}^{3+}$  within the lattice due to their proximity to one another(19). The cross-relaxation is not detrimental to the fundamental lasing transition because it aids in the population of the  ${}^3\text{F}_4$  upper-laser manifold. This process is responsible for nearly doubling the pump quantum efficiency(20) and is important because losses in radiative emission from the  ${}^3\text{F}_4$  manifold due to temperature increases within the sample can be avoided(9). The fundamental transition ( ${}^3\text{F}_4 \rightarrow {}^3\text{H}_6$ ) in  $\text{Tm}^{3+}$  is of particular importance because water has absorption bands at this wavelength. A laser operating at this wavelength may be applied in studies of the environment, body tissues and remote sensing (LIDAR)(21).

#### Co-Doped Materials

$\text{Tm}^{3+}$  may be introduced into various lattices with co-dopant ions such as  $\text{Cr}^{3+}$ ,  $\text{Ho}^{3+}$  and  $\text{Er}^{3+}$  with varying concentrations. Early studies by Johnson, *et al.*(1) have shown how co-dopant strategies can enhance laser performance. The IR emission from the  ${}^3\text{F}_4$  manifold to the ground state near  $5,200 \text{ cm}^{-1}$  in 1 atomic %  $\text{Tm}^{3+}:\text{YAG}$  was enhanced by a factor of 40 by replacing 50% of the yttrium ions in the YAG matrix with erbium ions.

Most often, when  $\text{Tm}^{3+}$  is used in a co-doped laser material, its role is to serve

as an energy transfer medium. Several studies have described the use of  $\text{Tm}^{3+}$  in YAG with  $\text{Ho}^{3+}$  and, or  $\text{Cr}^{3+}$  (20,22-29). One possible operating scheme is illustrated in Figure 3. When a  $\text{Cr}^{3+}$ ,  $\text{Tm}^{3+}$ ,  $\text{Ho}^{3+}$  co-doping scheme is employed, the  $\text{Cr}^{3+}$  ion is

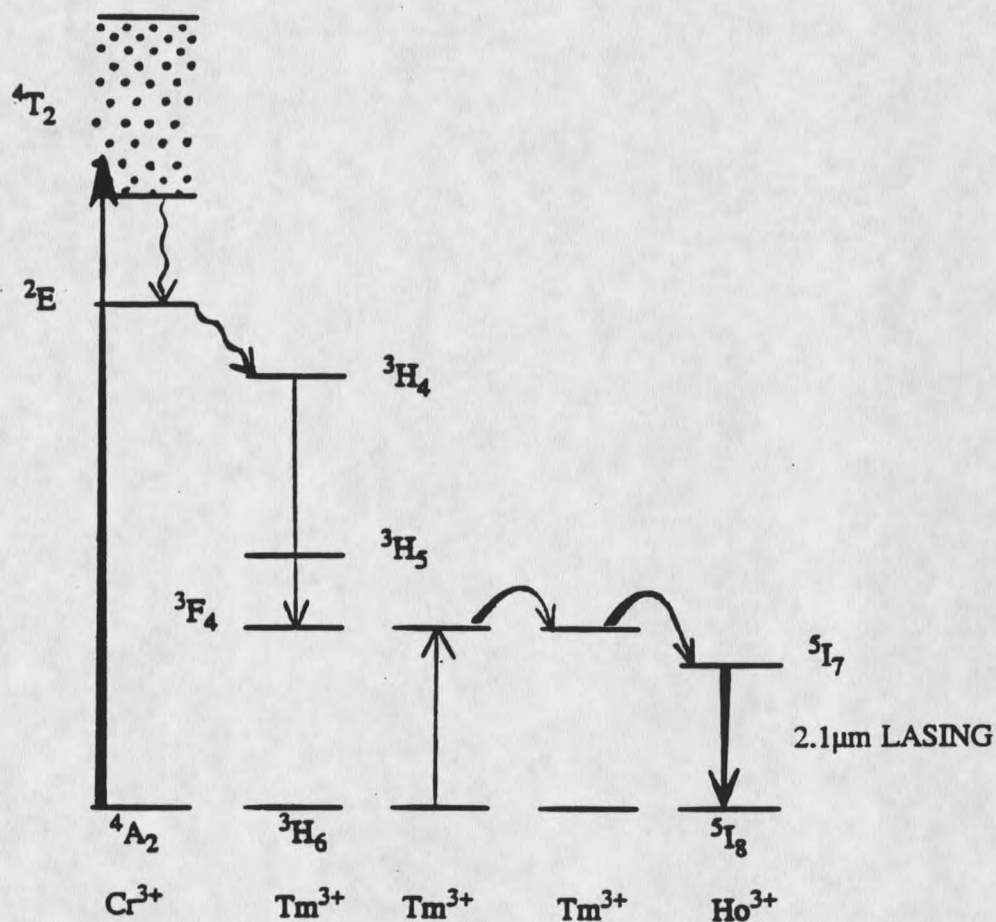


Figure 3. IR lasing operation scheme for CTH:YAG.

typically excited at an energy of approximately  $16,000 \text{ cm}^{-1}$ . This is followed by non-radiative decay to the  $\text{Cr}^{3+}$   $^2E$  manifold where there is sufficient overlap with the  $^3H_4$  manifold of  $\text{Tm}^{3+}$ . Energy is transferred to the  $^3H_4$  manifold predominantly non-

radiatively. Just as in  $\text{Tm}^{3+}$ :YAG energy decays to the  $^3\text{F}_4$  manifold and the cross-relaxation process in  $\text{Tm}^{3+}$  leads to the formation of two  $^3\text{F}_4$  states. Energy is then transferred from the  $^3\text{F}_4$  states to the  $^5\text{I}_7$  Stark manifold of  $\text{Ho}^{3+}$  followed by radiative emission to the  $^5\text{I}_8$  ground state.

It has been suggested that due to the inability to pump  $\text{Tm}^{3+}$  and  $\text{Ho}^{3+}$  efficiently with a broad-band source,  $\text{Cr}^{3+}$  must be utilized as the excitation medium to initiate the energy transfer process(23). Using a transition metal as a dopant ion is convenient because they typically exhibit broad absorption features and absorb a large fraction of excitation energy which is then available for transfer to a co-doped ion. A simple demonstration can show this process indirectly. When broad-band light is shown onto  $\text{Cr}^{3+}$ :YAG red light can be observed at the edges of the crystal exhibiting the radiative emission from the  $^4\text{T}_2$  manifold to the  $^4\text{A}_2$  ground state. However, when broad-band light is shown onto a crystal containing both  $\text{Cr}^{3+}$  and  $\text{Tm}^{3+}$ , red emission is not observed at the edge of the crystal. This is due to the fact that energy is being readily transferred to the  $\text{Tm}^{3+}$  via  $\text{Cr}^{3+}$  because of sufficient overlap between the  $\text{Cr}^{3+}$  emission and the corresponding absorption bands of  $\text{Tm}^{3+}$ (22).

Generally, when these types of crystals are grown they contain all three dopant materials. This allows the user greater flexibility when deciding which operating scheme to exploit. For example,  $\text{Cr}^{3+}$ , which has a broad visible absorption, may be more easily pumped by a visible source, as opposed to the  $\text{Tm}^{3+}$  ion. Consequently, due to the different excitation methods, and, in turn, slightly different energy transfer processes, observed emission intensities and lifetimes may deviate significantly. This may be

desirable depending on how the laser will be used. The materials described above are of interest for use in solid-state systems because of their extremely long radiative lifetimes in the IR. These long lifetimes might permit the storage of a large amount of energy which is beneficial for use in pulsed laser systems(20).

## CHAPTER 2

## TIME-RESOLVED FOURIER TRANSFORM SPECTROSCOPY

Background

Standard Fourier transform infrared (FT-IR) and Fourier transform visible spectroscopy (FT-VIS) have been used in many analytical studies for the determination of specific absorption wavelengths characteristic for a particular material. FT spectroscopy (FTS) became a confidently used and accepted analytical technique in the late 1960's due to previous findings made by Fellgett and Jaquinot, as well as, the availability of computers (quick data reduction) and helium-neon lasers (moving mirror monitoring)(30). FT-IR absorption spectroscopy is a powerful tool in the study of organic compounds. Through detailed analysis of standard samples, functional groups such as ketones, ethers, and amines have been "fingerprinted", that is, their spectra reveal characteristic absorption bands at certain frequencies and, also, a unique band structure which aids in the structural elucidation of molecules.

FTS has many advantages over other spectroscopic techniques. Fellgett determined that all of the components that make up a spectrum may be evaluated simultaneously. Due to this fact, the derivation of spectra using an FT spectroscopic

device is approximately *1000 times faster* than using a traditional spectrometer(31) due to the multiplex advantage. A short time later Jaquinot stated that an interferometer is relatively unlimited in the amount of radiation that may enter the instrument, hence the Jaquinot or throughput advantage.

Perhaps the only substantial disadvantage to using an FT interferometer is the initial investment made. Modern FT instruments are priced from approximately \$20,000 to \$200,000, or more in some cases. While the investment is substantial, it is believed that the efficiency of analysis will more than offset the initial monetary sacrifices.

#### Step-Scan FTS Technique

Temporal analysis of radiative emission can be accomplished through the use of time-resolved spectroscopy (TRS) via step-scan FT (FT-TRS). The first step-scan interferometer was developed in 1966(32). Widespread use of FT-TRS was not seen until very recently in the late 1980's and has only recently been applied to the analysis of laser materials(4,33). A recent study performed in 1996 concentrated on studies of transient chemical reactions using FT-TRS(34).

In order to perform step-scan measurements the instrument must function differently than in the normal rapid-scan mode. In the rapid-scan mode of analysis simultaneous collection of all the frequencies of light present at a given time takes place (spectral multiplexing). The moving mirror of the Michelson interferometer changes positions very rapidly at a velocity determined by the user, typically about 40kHz. This presents a problem for FT-TRS because there is no consideration of events occurring

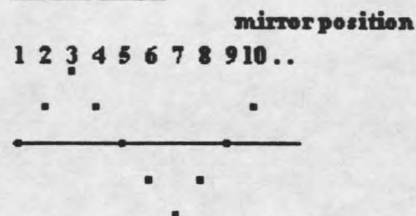
over time at every scheduled mirror position. As long as there exists a continuous emission, rapid-scan mode would suffice for frequency determination. Even when employing a modulated source, if the lifetime of the emission is sufficiently long-lived ( $> 1-2\text{ms}$ ), rapid-scan mode can characterize the frequency, but step-scan via FT-TRS is always required to characterize temporal events.

Temporal analysis is achieved by holding the moving mirror stationary at every mirror increment during data collection. In this way the spectral multiplexing can be separated from the time-based events that occur after pulsed excitation(35). In normal, rapid-scan FTS it is important to keep the moving mirror *velocity* constant while data are obtained, whereas, in step-scan FTS it is important to keep the moving mirror *position* constant to ensure accurately obtained information for Fourier transformation(35).

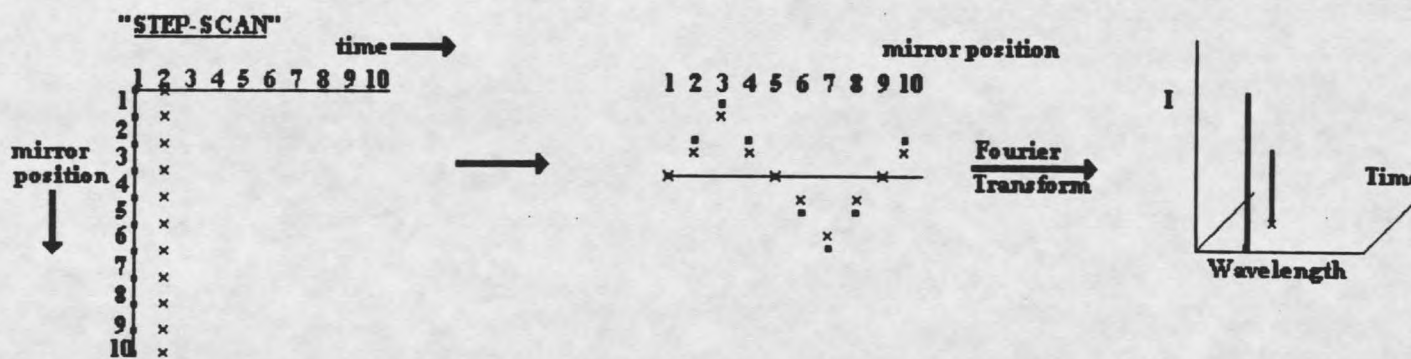
These requirements are shown in Figure 4. For the step-scan mode the moving mirror position is on the y-axis and the length of time (arbitrary units) the mirror is held at each position is on the x-axis. The length of time at each scheduled mirror position is determined by the duration (temporal resolution) and number of time intervals. Each vertical column contains the information needed to construct the single frequency interferogram at the corresponding time interval. It can be seen that a number of interferograms that contain time and intensity information will be assembled whose amplitude is decreasing over time. The waveforms will then be Fourier transformed to yield a FT-TRS spectrum. Figure 5 again shows the formation of each interferogram at every mirror position and conversion to the time-resolved spectrum.

## Formation of the Interferogram

### "RAPID SCAN"



- the instrument collects frequency information at certain mirror positions as it moves back and forth
- this information is digitized to yield the actual points that make up the interferogram
- the Fourier transform is then performed to yield the observed spectrum



\* - this model assumes one frequency only

Figure 4. Formation of the interferogram in rapid-scan mode vs. step-scan mode.

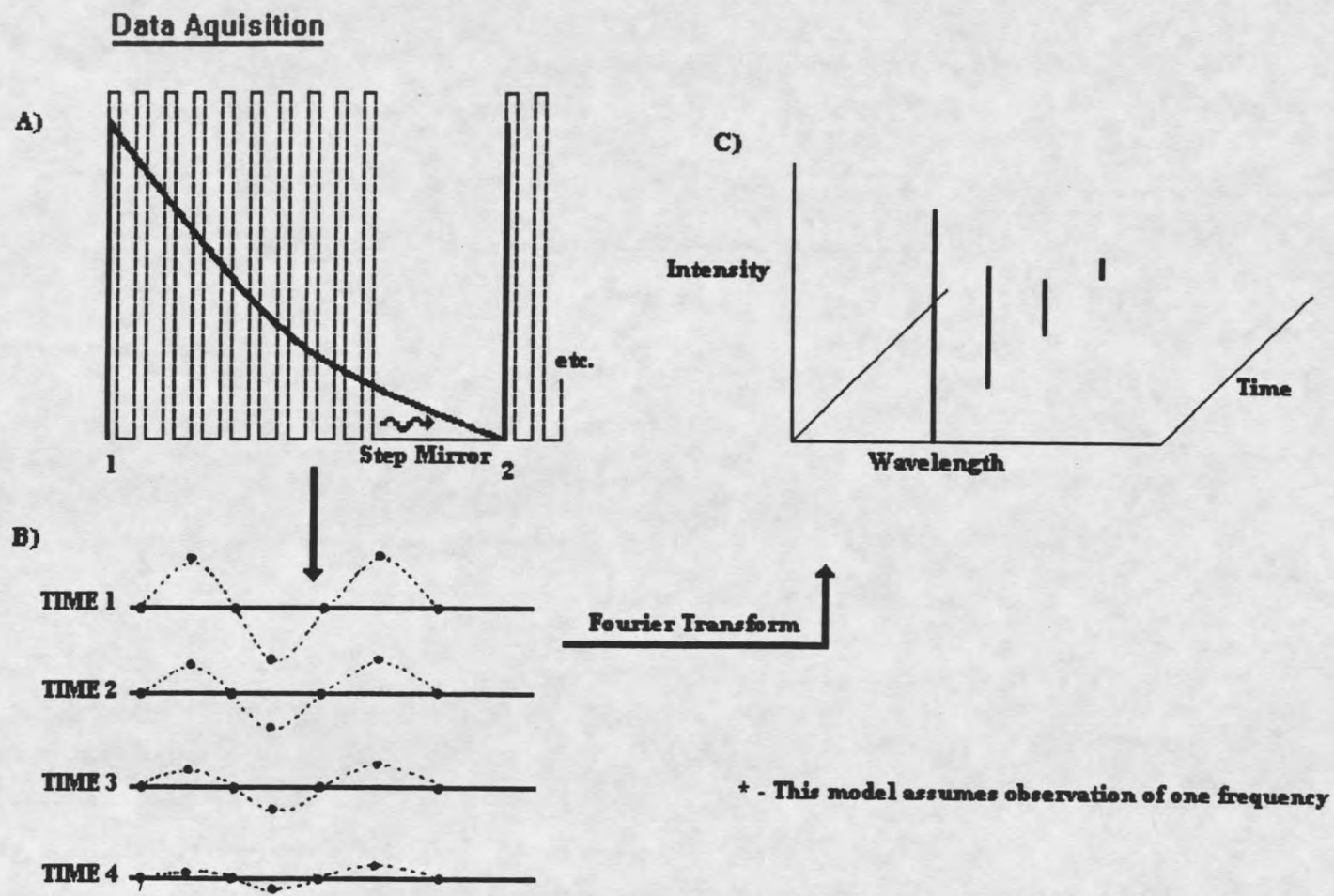


Figure 5. Derivation of the time-resolved spectrum.

### Normalization of FT-TRS and Inherent Spectral Noise

Upon examination of the FT-TRS spectra (Figure 6) one notices baseline noise which decreases proportionally with decreasing signal. This noise is due directly to pulse to pulse fluctuations in the pump laser output which are manifested in the emission from the sample material.

Figure 6 exhibits this noise for an emission in  $\text{Tm}^{3+}:\text{YAG}$ . The upper spectrum is obtained by exciting the sample continuously by 780 nm diode laser output. A relatively noise-free FT-TRS spectrum is obtained when no fluctuations in the laser pump power occur. By manually changing the pump power as the data is collected, noise is artificially created as seen in the lower spectrum. The noise is random in the energy regime, but shows consistency in intensity.

If we assume that a single frequency is being emitted and reaching the detector we can more easily see how this noise is created in the interferogram. If the emission is consistent from pulse to pulse a smooth single frequency interferogram is constructed as in Figures 4 and 5. When intensity fluctuations occur, significant amplitude differences occur at the points where data is obtained by the instrument which leads to the construction of a completely different interferogram comprised of several different frequencies, but still contains the emission frequency of interest. The ratio of the noise to the signal is constant over time which is evident in all of the FT-TRS spectra. This effect can be represented for a multi-frequency emission by comparing interferograms at a given time in the clean and noisy spectra as shown in Figure 7. The lower traces exhibit the difference between the magnitudes of the 2 interferograms and resultant

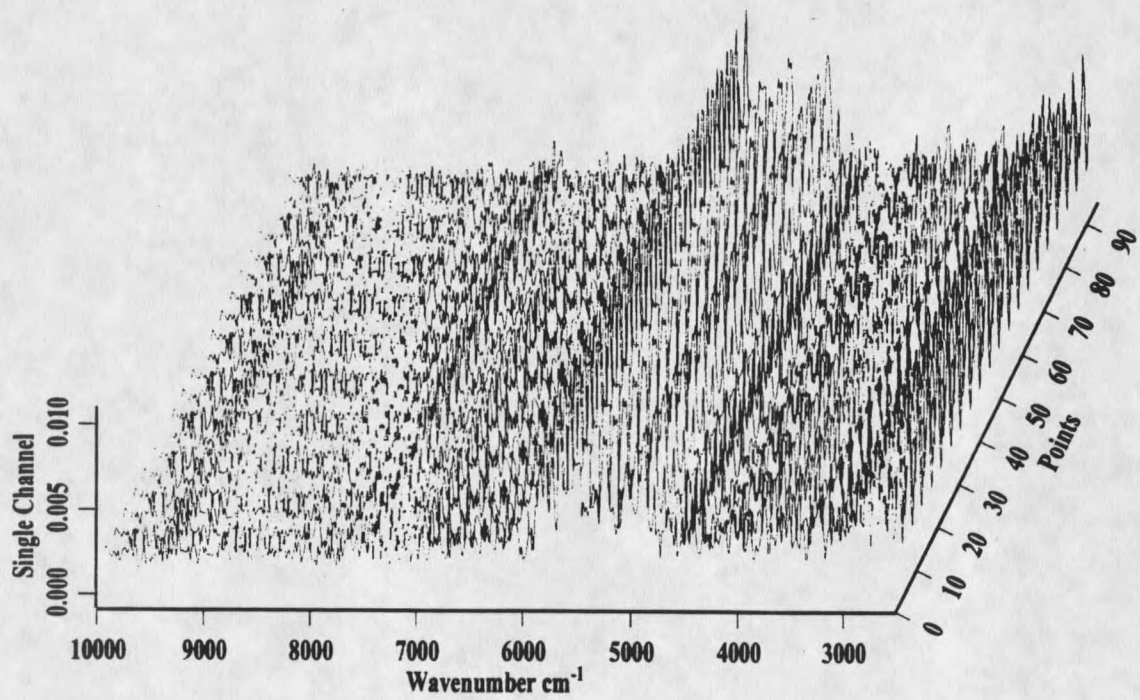
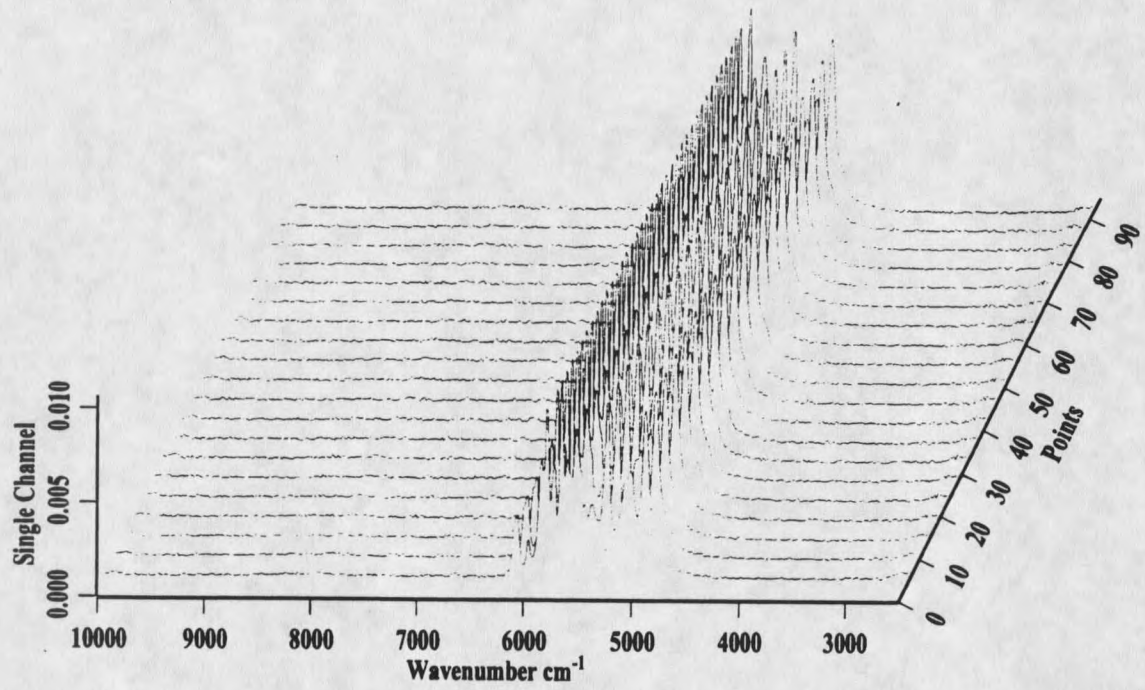


Figure 6. Generation of systematic noise in FT-TRS spectra.

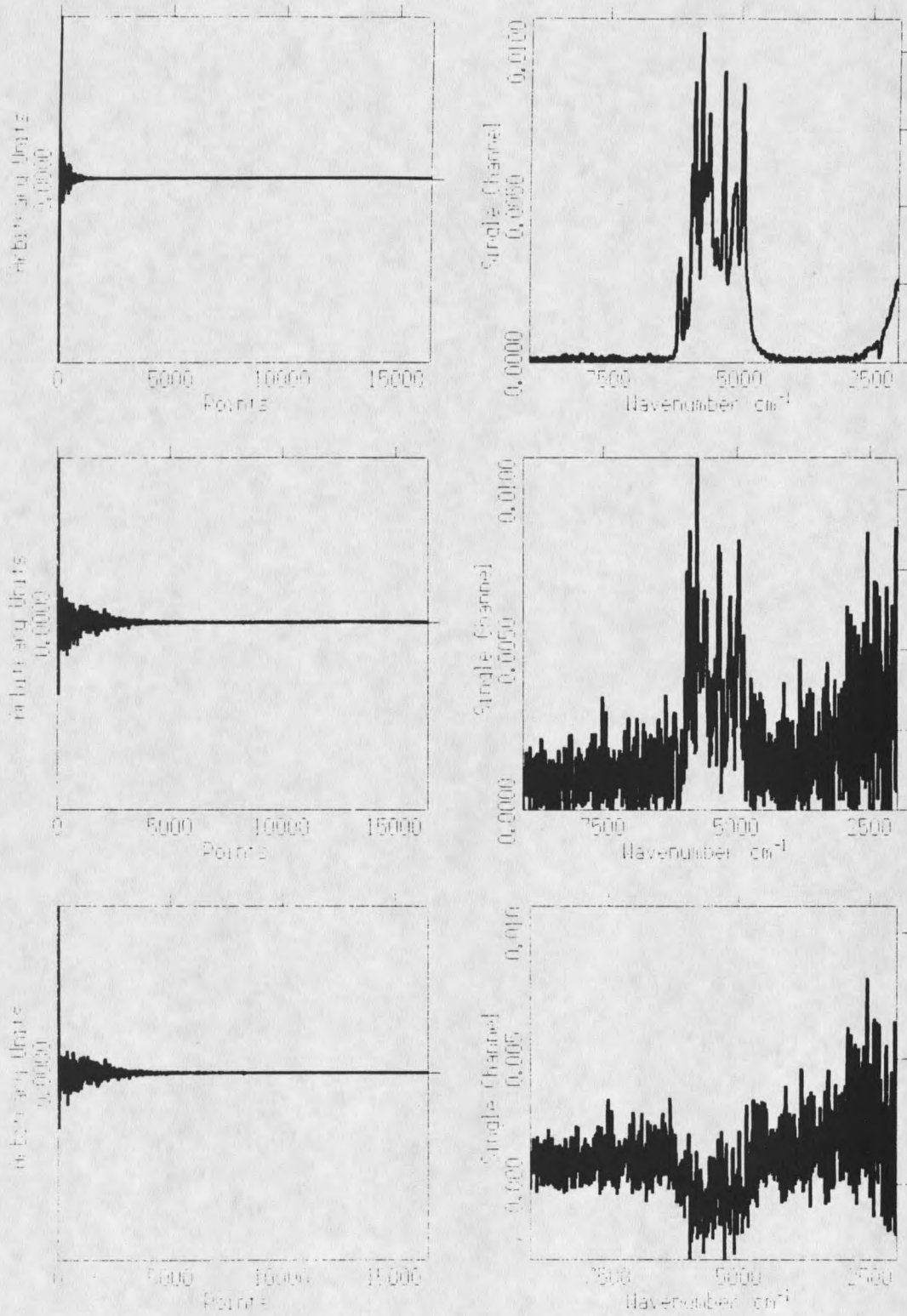


Figure 7. Interferograms and corresponding spectra.

noise upon Fourier transformation. The process of distributing the noise throughout the spectral region of study is perhaps a benefit, that is, the noise typically does not occur exclusively where emission signal is present. Consequently, for the more intense emission processes, useful information regarding emission lifetimes and frequencies may be obtained when there are significant pulse to pulse fluctuations. However, the ability to correct the interferogram at each time by considering a corresponding reference interferogram would allow for much clearer FT-TRS spectra and in turn more accurate integrations, emission trace extracts and lifetime determinations. IR normalization may require an additional detector for this region. Currently, this is a financial limitation which can be overcome in the near future.

#### FT-TRS Nomenclature

FT-TRS measurements performed in this study are described by specific nomenclature that corresponds to experimental parameters and spectral interpretation. The nomenclature is derived from the manufacturer software which controls the system. The following is a discussion of the terms used in FT-TRS. Figure 8 will be used as the reference step-scan spectrum for this discussion.

Each emission trace (spectrum) represents a "time slice" or more descriptively, the time interval between data sampling at each mirror position (temporal resolution). There is no theoretical limit on the number of time slices that may be taken for an experiment, however we are limited by computer datafile space. The spectrum in Figure 8 contains 200 time slices with 500  $\mu$ sec temporal resolution. The magnitude of the

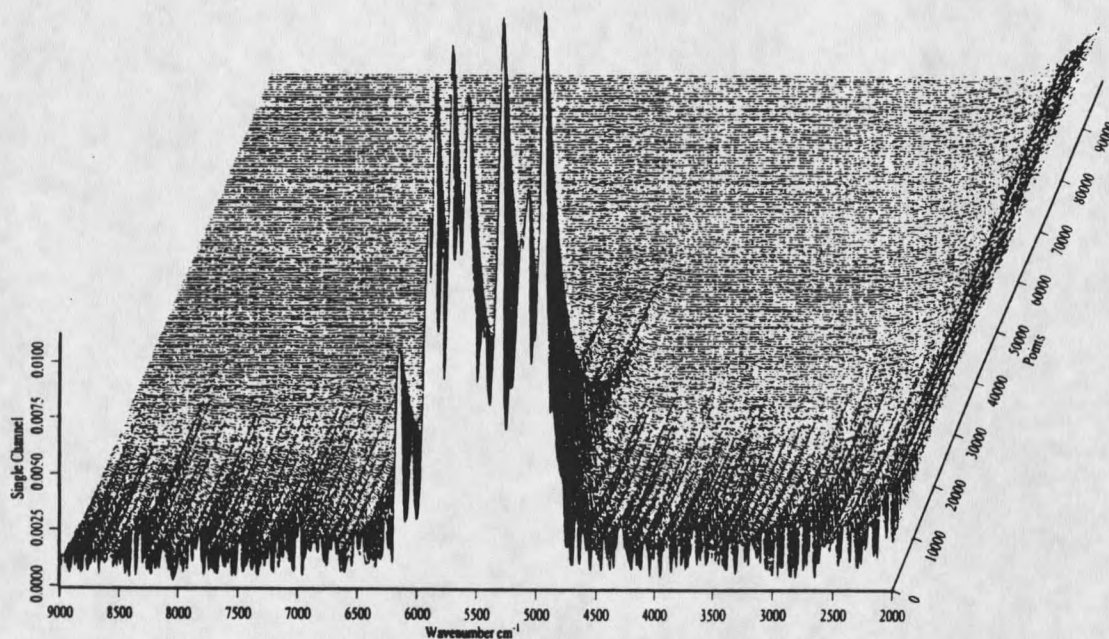


Figure 8. A step-scan emission spectrum.

temporal resolution paired with the number of time slices determines the length of emission sampling ( $100,000 \mu\text{sec}$ ). The signal to noise (S/N) ratio can be improved by a signal averaging technique known as co-adding. If 20 co-additions are selected the instrument will hold the moving mirror at a given position for 20 laser pulses before moving to the next mirror position. Consequently, 20 values that describe emission intensity and mirror position for each time slice will be obtained and averaged yielding a single point in each interferogram.

The IFS 66 has 2 different modes for acquiring time-resolved data. The internal ADC (IADC) mode is a 16-bit analog to digital converter that is used for studying emission events which occur in the  $\mu\text{sec}$  to msec regime. The maximum temporal resolution for IADC mode is  $5 \mu\text{sec}$ . The electronics for IADC can process signals from

the detector with voltages that range from 0 to  $\pm 15$  V. Typically, 10 to 12 V from the detector is rarely exceeded and no adjustments (aperaturing, for example) to the experimental design are necessary to ensure that the detector is not being saturated due to sample emission alone. The PAD82 mode uses a faster 8-bit analog to digital converter and has a maximum temporal resolution of 5 nsec and a minimum resolution of 8  $\mu$ sec. However, the electronics that govern PAD82 require an input voltage from the detector of less than +1 V and more than 0 V. If the voltage does not fall within this specified range a usable, coherent spectrum cannot be obtained and, therefore, a more cautious approach to obtaining data is required.

## CHAPTER 3

### EXPERIMENTAL PROCEDURE

Aspects of experimental design, apparatuses, samples and procedures are outlined and presented in this chapter. Also, the stepwise method of laser material analysis is described, as well as modifications to the interferometer and the integration of light collecting optics to the experimental setup.

#### Sample Laser Materials

All crystalline laser materials used to acquire experimental results were obtained from Scientific Materials Corporation located in Bozeman, Montana. The materials used were shown to be of sufficient purity through absorption measurements and in good physical condition.

The concentrations of the dopant ion in the respective samples are as follows: 5  $\text{Tm}^{3+}$  doped YAG crystals at 0.1, 0.25, 2.4, 4.0 and 5.2 atomic percent, 2  $\text{Tm}^{3+}$  doped  $\text{YAlO}_3$  (YALO) crystals at 0.1 and 4 atomic percent, 2  $\text{Tm}^{3+}$  doped  $\text{Y}_2\text{SiO}_5$  (YSO) crystals at 0.1 and 3 atomic percent, 2  $\text{Tm}^{3+}$  doped  $\text{Y}_2\text{O}_3$  (YO) crystals at 0.1 and 3 atomic percent, and 1  $\text{Tm}^{3+}$  doped  $\text{Lu}_3\text{Al}_5\text{O}_{12}$  (LAG) crystal at 2 atomic percent. In

each case,  $\text{Tm}^{3+}$  substitutes for yttrium or lutetium.

The samples are generally rectangular or circular ranging in size from quarter to a sixteenth of an inch in thickness and an eighth of an inch to 1 inch in diameter or length. Most of the samples have polished edges. The  $\text{Tm}^{3+}:\text{YO}$  samples are a noted exception. Due to the complexity of the growing process, these samples are very small and lack uniformity. The samples are cleaned with high purity acetone prior to analysis to remove residues that may have accumulated on the surfaces.

### Experimental Apparatus

The apparatus used for both absorption and emission experiments is shown in Figure 9. In all experiments a Bruker Instruments IFS 66 step-scan interferometer was used to obtain and analyze visible and infrared radiation (see Figure 10).

The IFS 66 consists of a Michelson interferometer using a HeNe laser for internal mirror positional referencing. The reference wavelength is  $15,879.8 \text{ cm}^{-1}$  (632.99 nm). The maximum resolution for the IFS 66 is  $0.1 \text{ cm}^{-1}$ . The beamsplitters (BS, Figure 10) used for visible and infrared studies are respectively, quartz and calcium fluoride ( $\text{CaF}_2$ ). Spectral ranges for these beamsplitter/detector combinations are shown in Figure 11. The device used for infrared measurements is a liquid nitrogen cooled Graseby-Specac indium antimonide (InSb) detector (D2, Figure 10) coupled with an external pre-amplifier that has a 120 nsec risetime and 60 nsec recovery time. The InSb/ $\text{CaF}_2$  detector/beamsplitter combination is capable of detecting emitting wavelengths from nearly  $16,000\text{-}2,000 \text{ cm}^{-1}$ . The detector used for visible measurements is a silicon diode

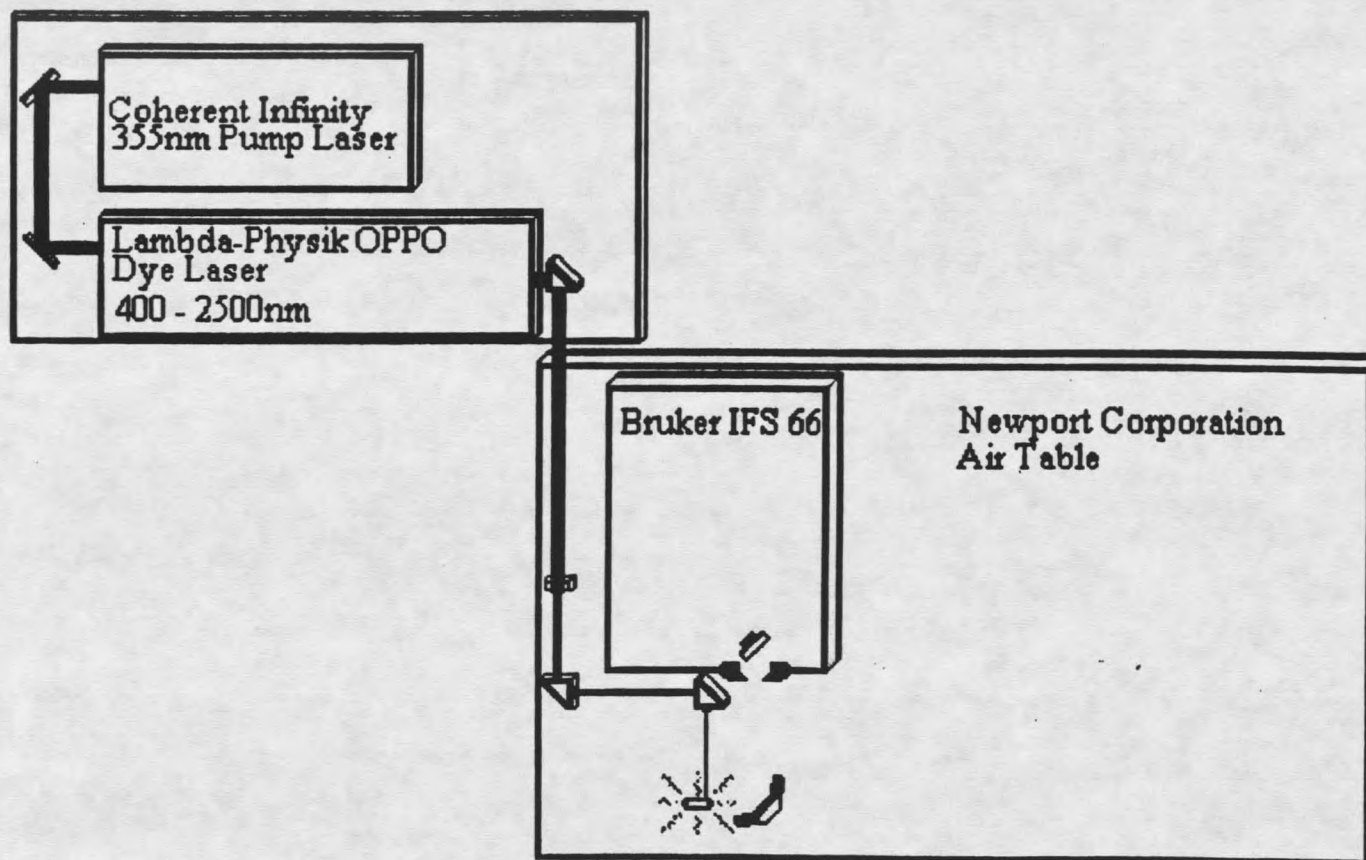


Figure 9. Apparatus for absorption and emission studies.

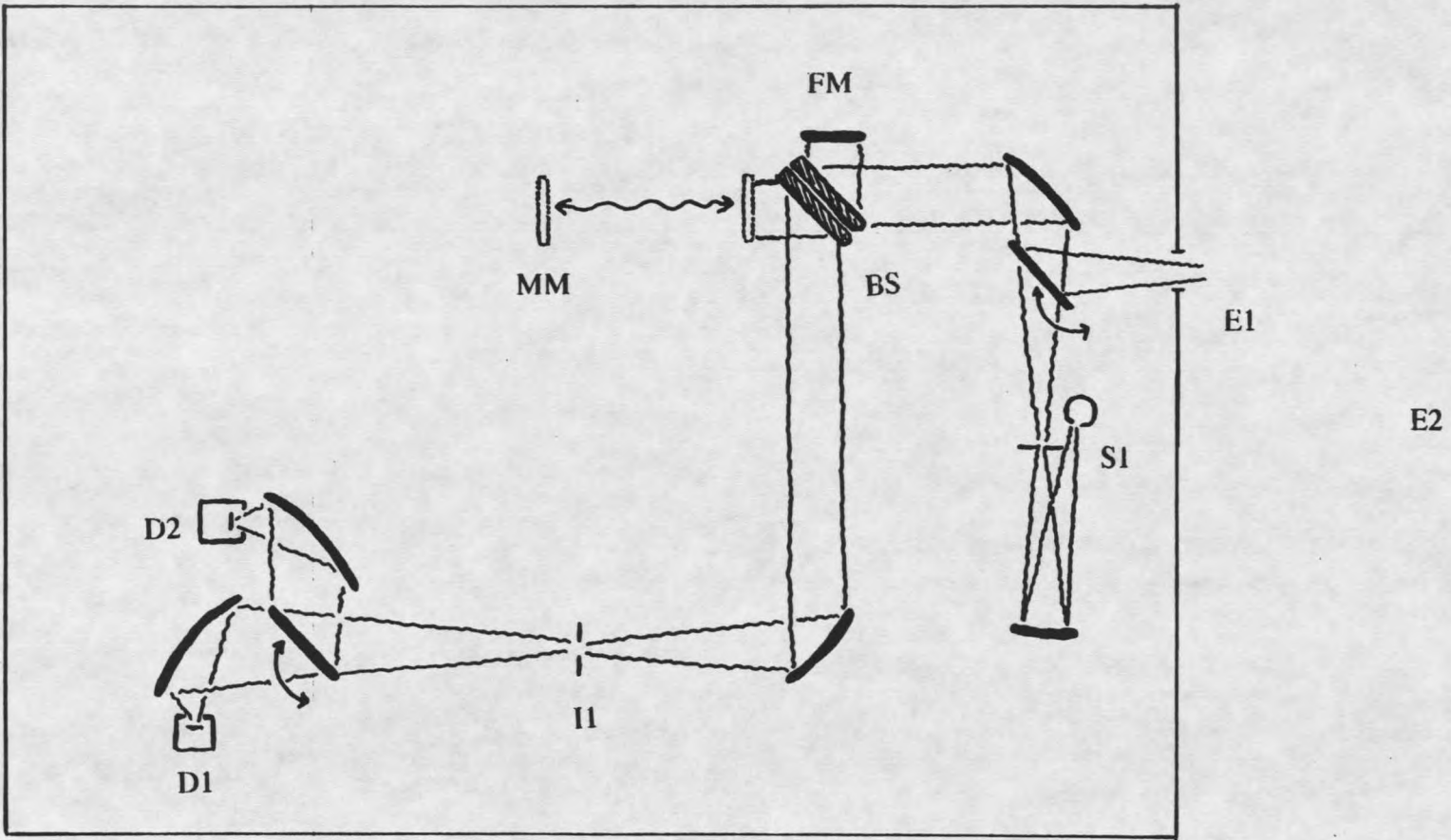


Figure 10. The Bruker IFS 66 step-scan interferometer.

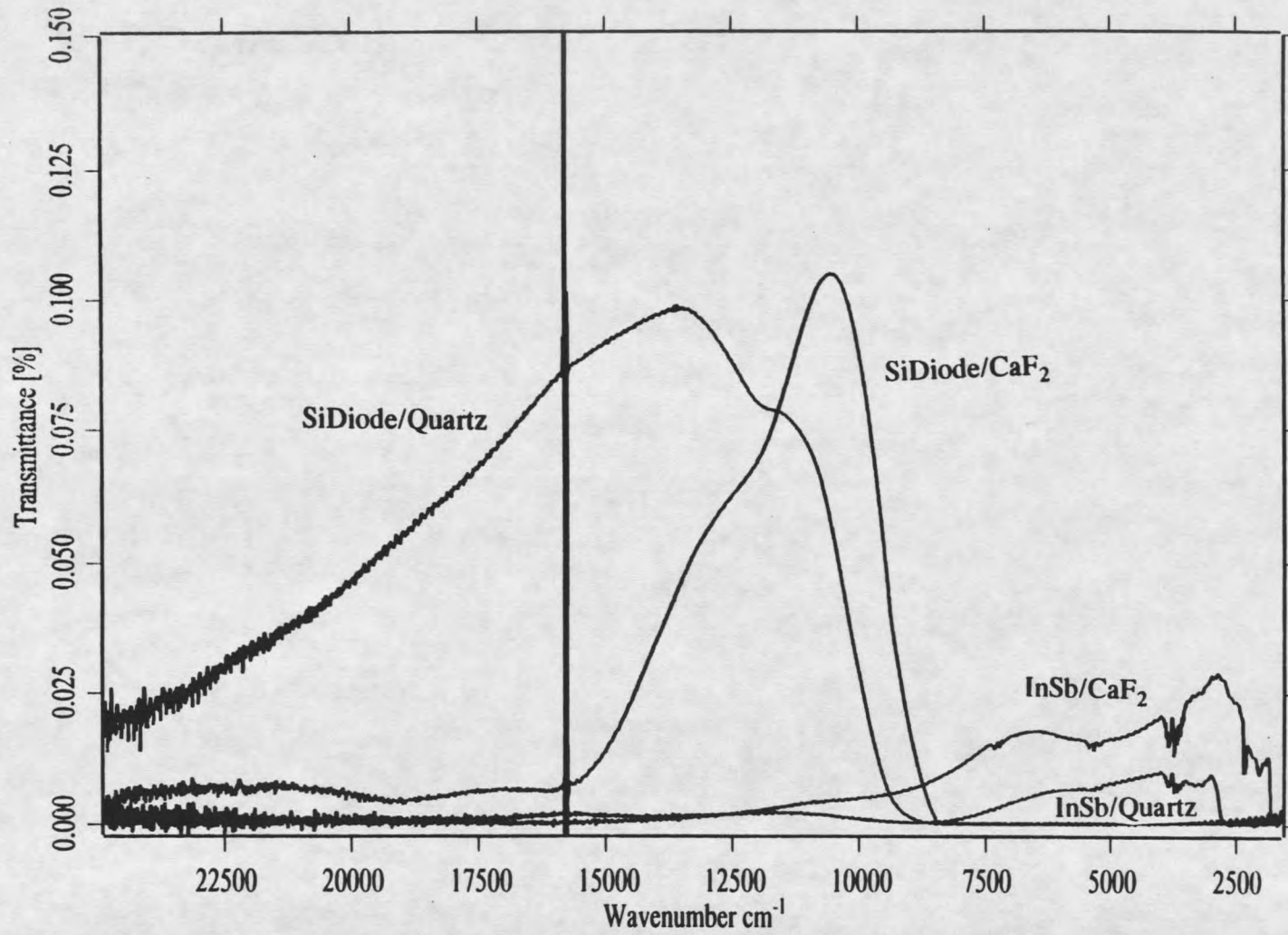


Figure 11. Spectra for detector/beam splitter combinations.

(D1, Figure 10) obtained from Bruker Instruments. This diode has a built in pre-amplifier with a rise and recovery time of 15 and 25 nsec, respectively. Rise and recovery time measurements were performed by passing a scattered laser pulse of known wavelength through the interferometer and then measuring the temporal response of the detector in relation to the pulse. The Si/Quartz detector/beamsplitter combination can detect radiative emission from nearly 27,000-9,000  $\text{cm}^{-1}$ .

All absorption measurements were made using a tungsten lamp (S1, Figure 10) as the source of visible and IR radiation.

The  $^3\text{H}_4$  Stark manifold of  $\text{Tm}^{3+}$  readily absorbs radiation supplied by an Opto Power Corporation CW diode laser operating near 12,800  $\text{cm}^{-1}$  (see Figure 2). Initial FT-TRS experiments were performed by modulating the diode output beam with a PTI mechanical chopper that, at 100 Hz, provided a pulse of 1 msec duration with relatively long rise and fall times. The beam diameter was 0.25 inches at the sample and was not focused.

A shorter pulse was necessary to more accurately model crystal behavior within an actual operating laser system. Currently, a Coherent Infinity 40-100 series Nd:YAG laser operating at the third harmonic (355 nm) is used to pump a Lambda-Physik OPO which, in turn can generate wavelengths of 400 nm to nearly 2.5  $\mu\text{m}$ . The Infinity is capable of operating at 0.1 to 100 Hz repetition rate with a pulse duration of approximately 8nsec. The third harmonic's output intensity at 10 Hz repetition and 425 mJ fundamental (1064 nm) is approximately 2.0 W and at a higher repetition rate of 100 Hz and 375 mJ fundamental intensity the 355 nm output is approximately 16 W. The

linewidth of the 355 nm output is typically less than  $0.008 \text{ cm}^{-1}$ . The 355 nm beam is turned by two dichroic mirrors obtained from Newport Corporation into the Lambda-Physik Scanmate OPO. Amplified tunable laser output is then achieved through the use of the Scanmate. The "signal" (410-710 nm) and "idler" (710-2446 nm) beams allow for excitation over a broad wavelength region. The signal beam for this system is typically 10 times more powerful than the idler, 20 to 30 mJ/pulse compared to 2.0 to 5.0 mJ/pulse. Filters supplied by Lambda-Physik allow the user to select the signal or idler for sample excitation. An RG715 filter is nearly 0% transmissive to wavelengths shorter than 714 nm ( $14,000 \text{ cm}^{-1}$ ) (see Figure 12) allowing for elimination of the signal output from many dyes. An KG3 filter is nearly 0% transmissive to IR wavelengths below  $12,000 \text{ cm}^{-1}$  in energy, but passes visible radiation.

The output of the OPO is immediately turned by a fused silica prism obtained from Virgo Optics and focused to a beam diameter of approximately 2 mm at the sample by an f/12 lens. Samples are typically placed at the focal point incident to the beam at an edge to allow for maximum absorption of pump light and to minimize the effects of self-absorption or radiation trapping. Light emitting from the edge of the sample is then collected. Radiation trapping within a material can change the bandshape of the observed emission spectra and also lead to spuriously long lifetimes(36). The pump beam must also contact the volume of the material that is at the focal point, again to diminish the self-absorption process.

Light emission is collected and focused into the interferometer by an off-axis paraboloid mirror (f number=4.5) obtained from Bruker Instruments. Light enters the

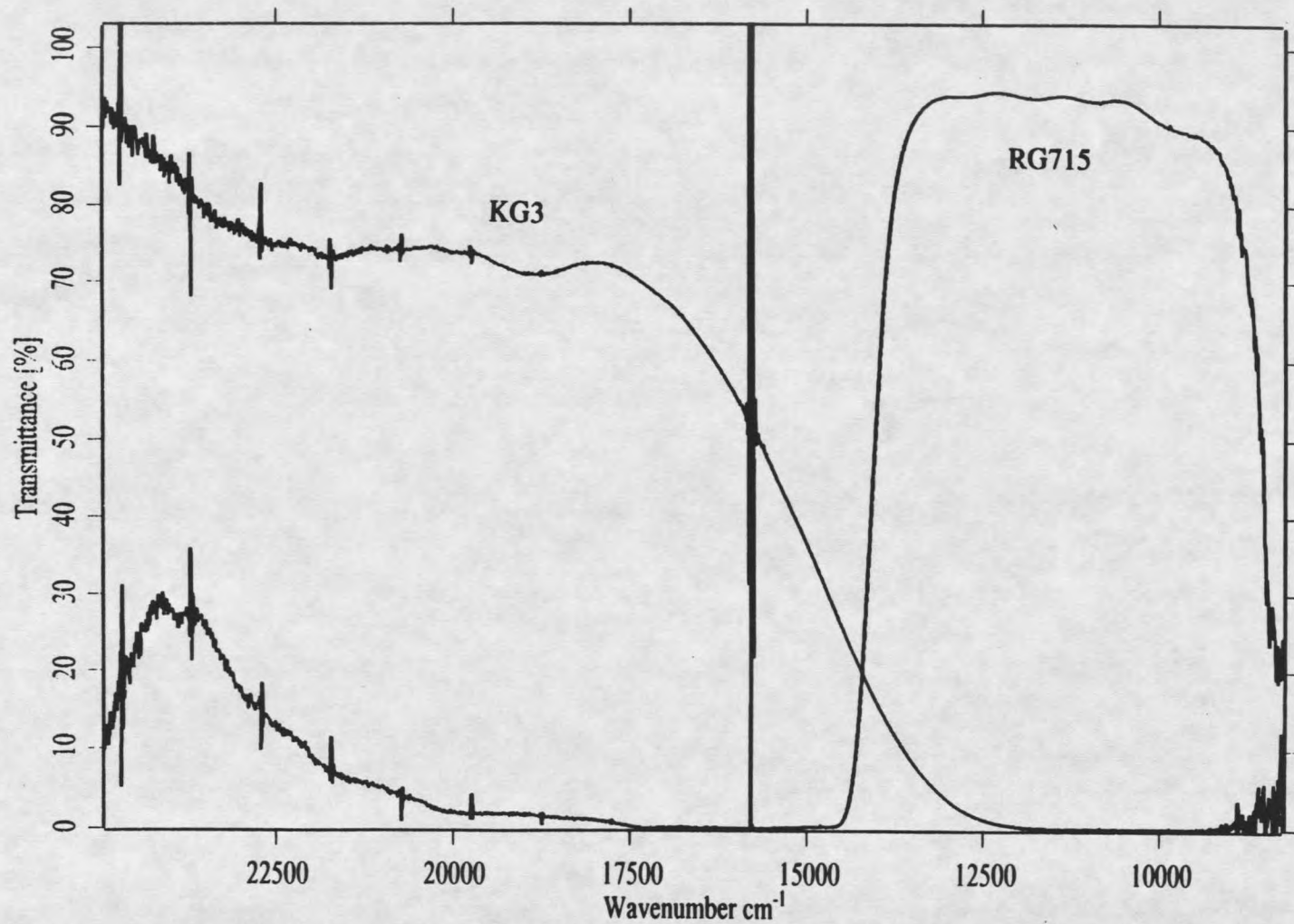


Figure 12. Spectra for KG3 and RG715 optical filters.

instrument through the entrance at E1, is turned at the internal flipping mirror of the interferometer and proceeds through the instrument to the corresponding detector. For IR measurements performed in the 9,000-2,000  $\text{cm}^{-1}$  range an Si filter is placed at E1. This filter eliminates nearly 100% of wavelengths less than 9,000  $\text{cm}^{-1}$  and is approximately 50% transmissive to wavelengths greater than 9,000  $\text{cm}^{-1}$ . The RG715 filter is placed at I1 if the visible OPO beam is being used for excitation to eliminate visible wavelengths prior to reaching the InSb detector. Measurements performed from 14,000-2,000  $\text{cm}^{-1}$  requires that only the RG715 filter be placed at E1.

Synchronization of the moving mirror to the excitation pulse is accomplished by triggering the IFS with TTL signals provided directly from the Infinity pump laser.

### The Material Characterization Process

Upon receiving a sample laser material a series of steps are followed for complete characterization. Absorption spectra in both the visible and IR regions of the wavelength spectrum are obtained with sufficient resolution ( $<2.0 \text{ cm}^{-1}$ ) and signal averaging ( $>1000$  scans). This allows the user to determine which Stark levels may be pumped to initiate energy transfer.

It is also beneficial to next obtain a continuous emission spectrum of sufficient resolution (typically,  $8.0 \text{ cm}^{-1}$ ) if the sample possesses an absorption band that may be excited by an available continuous source. This allows identification of the strongest emission band(s). It may then be assumed that this emission has a relatively long lifetime ( $>5 \mu\text{sec}$ ). This determination is important because the instrument uses the two

aforementioned methods for acquiring FT-TRS data.

The last step of the characterization is finding the lifetimes of the radiative energy transfer processes. Generally, IADC is performed first and then temporal resolution is increased to "see" the faster processes that are occurring in the material and PAD82 becomes necessary for analysis.

## CHAPTER 4

### EXPERIMENTAL RESULTS

In this section data will be presented and briefly interpreted. Chapter 5 contains detailed discussion of the FT-TRS data, as well as the model generated to describe the kinetics of the materials studied and the theory upon which the model is based.

#### Absorption Spectra

Absorption spectra and energy levels for  $\text{Tm}^{3+}$  doped into various materials at liquid helium or liquid nitrogen temperatures have been reported previously(37-41) and are of importance when making room temperature assignments. All absorption measurements in this study were performed at room temperature. Typically, absorption measurements made with the IFS 66 are resolved to  $2.0 \text{ cm}^{-1}$ . The number of scans performed (signal averaging) varies from 64 to 4096 depending on the desired S/N ratio. For  $\text{Tm}^{3+}$ :YAG materials, a sample of undoped YAG is employed for the background measurement with which the sample measurement is divided by to eliminate the spectral contributions caused by entities other than the  $\text{Tm}^{3+}$  ion. A tungsten source was used for measurements for both the IR region ( $9,000$  to  $2,000 \text{ cm}^{-1}$ ) and the visible region

(23,000 to 9,000  $\text{cm}^{-1}$ ). The observation of phonon absorption due to the crystalline lattice was not possible as these absorptions most often occur below 2,000  $\text{cm}^{-1}$ (37). The decrease in detector/beamsplitter response drastically diminishes the S/N ratio outside of the stated wavelength regions.

Absorption measurements were performed on all samples, but only the spectra for 4%  $\text{Tm}^{3+}$ :YAG, 4%  $\text{Tm}^{3+}$ :YALO, 3%  $\text{Tm}^{3+}$ :YSO and 3%  $\text{Tm}^{3+}$ :YO are shown because spectra for a given host crystal exhibit similar absorption features regardless of concentration. A correction was performed to eliminate baseline deviations across the spectrum so that the magnitudes of the absorptions could be compared between manifolds.

Absorption spectra are presented in Figures 13 through 17. The IR absorption spectrum for each sample is shown prior to the visible spectrum. The spectra exhibit the characteristic sharp line shapes of f electron transitions in rare-earth doped laser materials. Comparing the absorption spectra for  $\text{Tm}^{3+}$ :YAG to data obtained by Gruber, *et al.*(37) at 90 K reveals small shifts in maximum absorption energies. Gruber, *et al.*(37) report the energies for absorption maxima of the  $^1\text{G}_4$ ,  $^3\text{F}_3$ ,  $^3\text{H}_4$ , and  $^3\text{F}_4$  manifolds to be 21,757  $\text{cm}^{-1}$ , 14,679  $\text{cm}^{-1}$ , 12,720  $\text{cm}^{-1}$  and 5,901  $\text{cm}^{-1}$ , respectively. These room temperature measurements show maxima occurring at 21,742  $\text{cm}^{-1}$ , 14,680  $\text{cm}^{-1}$ , 12,724  $\text{cm}^{-1}$  and 6,146  $\text{cm}^{-1}$  for the same manifolds. The room temperature spectra are considerably less resolved than the spectra obtained at low temperatures. Spectral broadening can be attributed to the upper levels of the ground state manifold being thermally populated leading to a larger number of absorption pathways from the

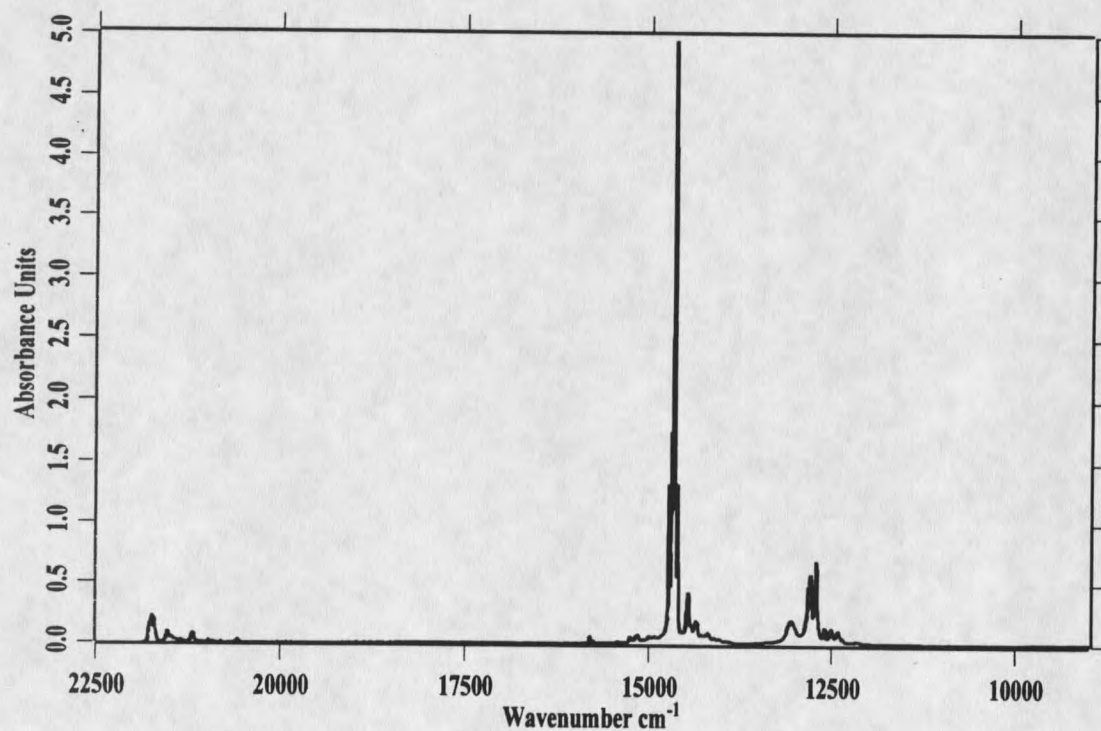
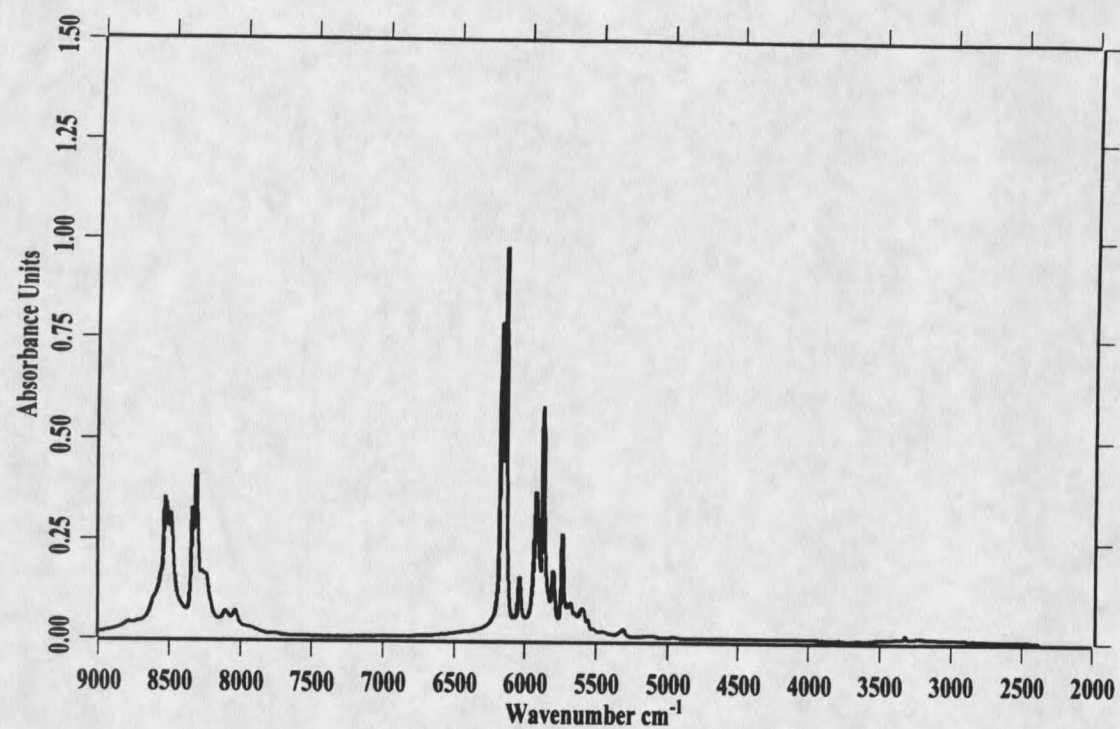


Figure 13. IR (top) and visible absorption spectra for  $\text{Tm}^{3+}:\text{YAG}$ .

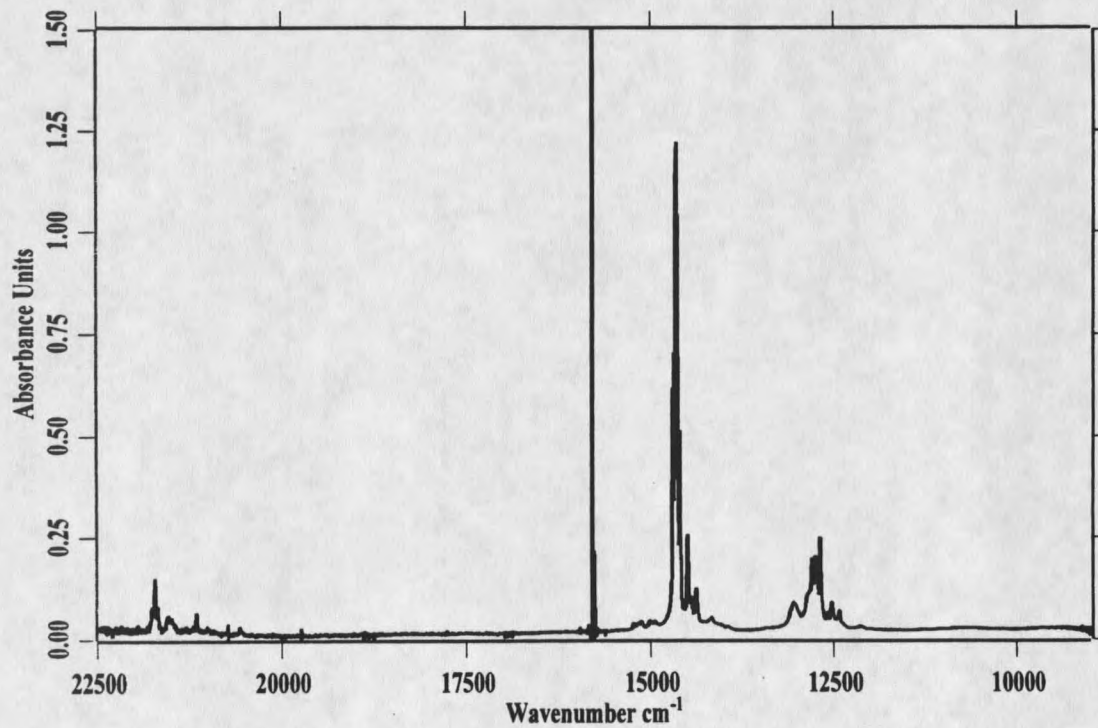
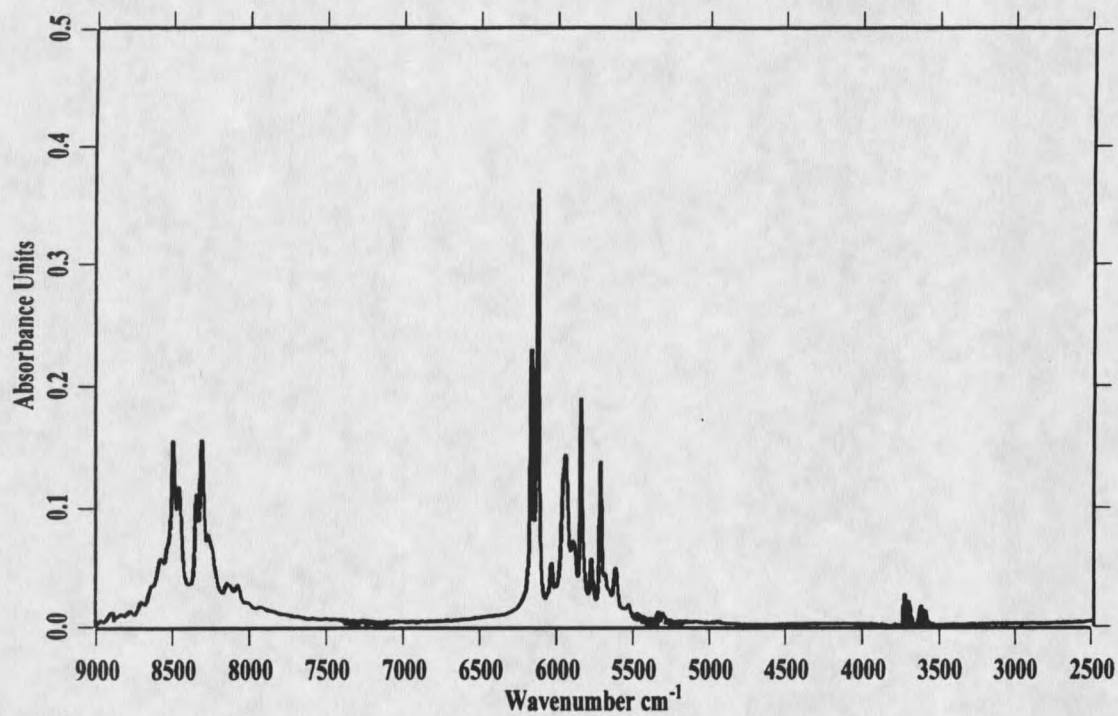


Figure 14. IR (top) and visible absorption spectra for  $\text{Tm}^{3+}:\text{LAG}$ .

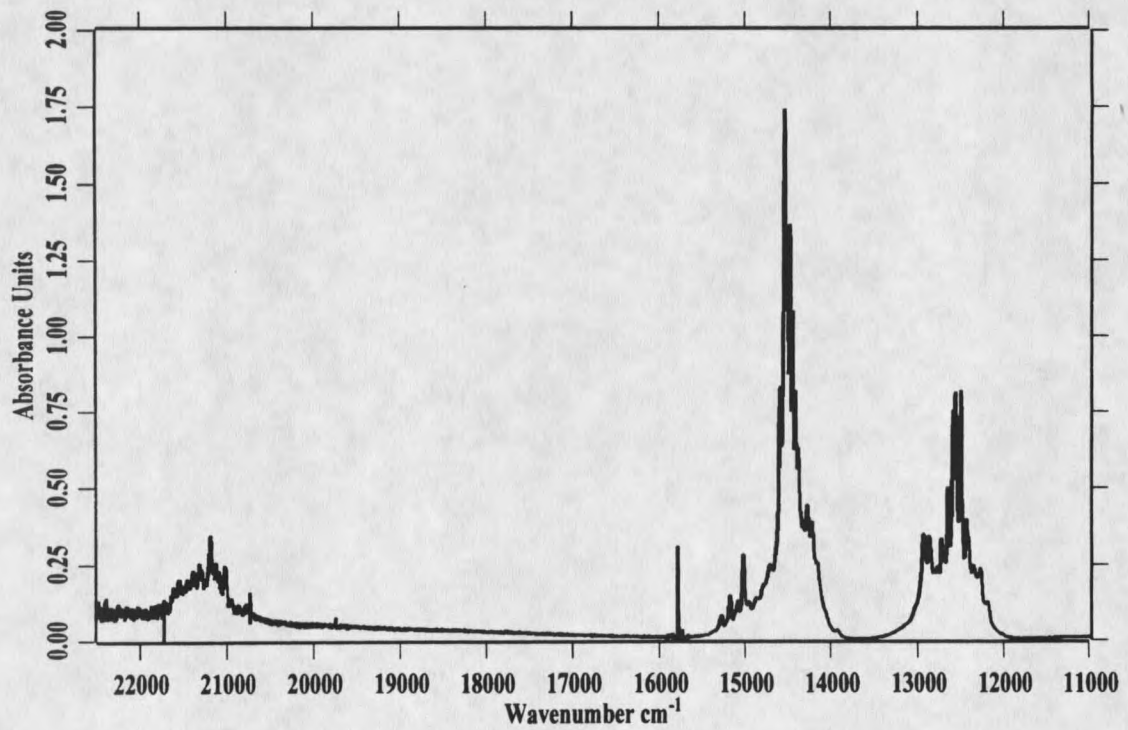
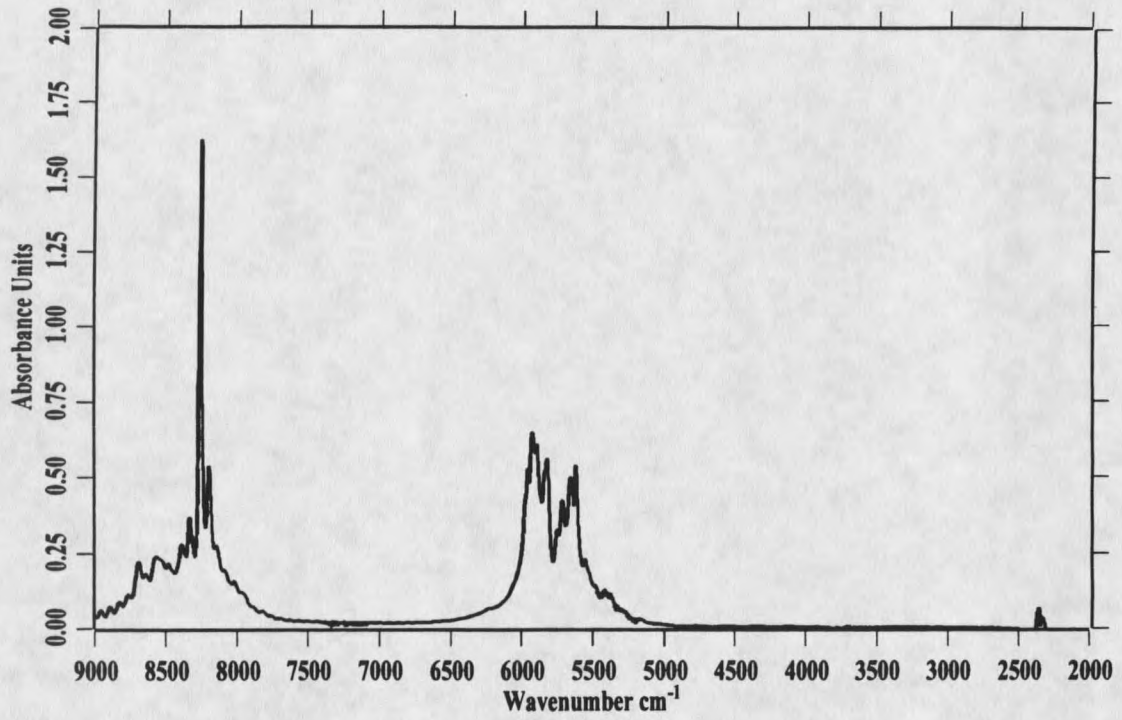


Figure 15. IR (top) and visible absorption spectra for Tm<sup>3+</sup>:YALO.

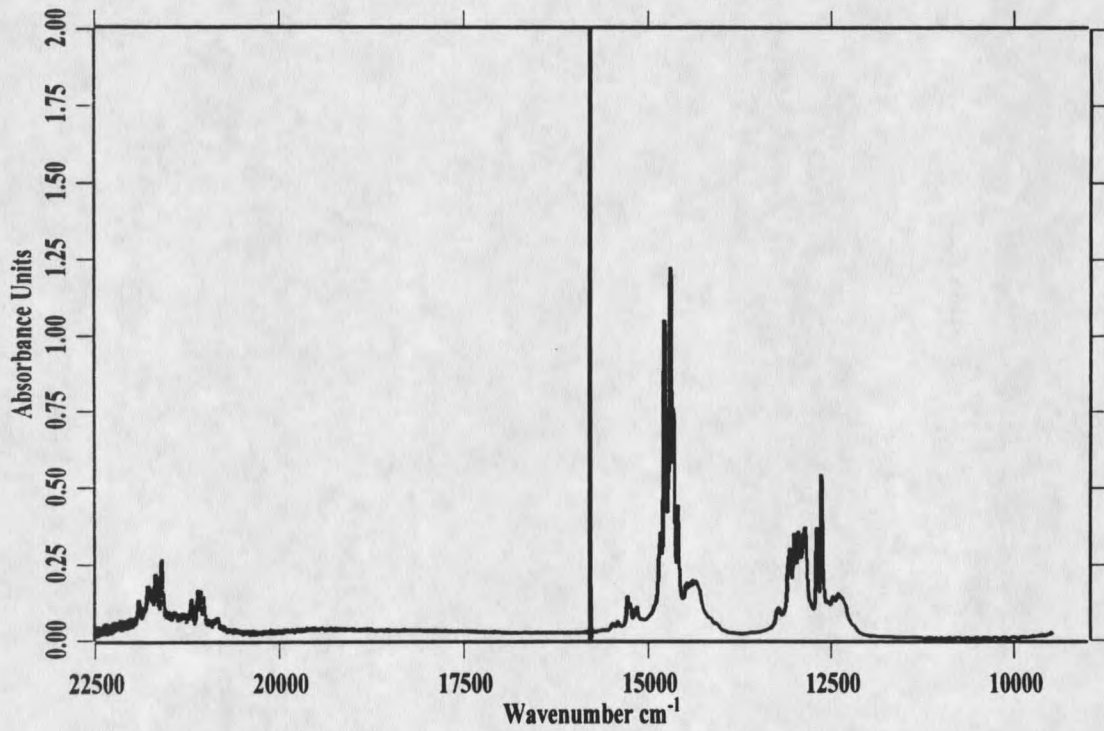
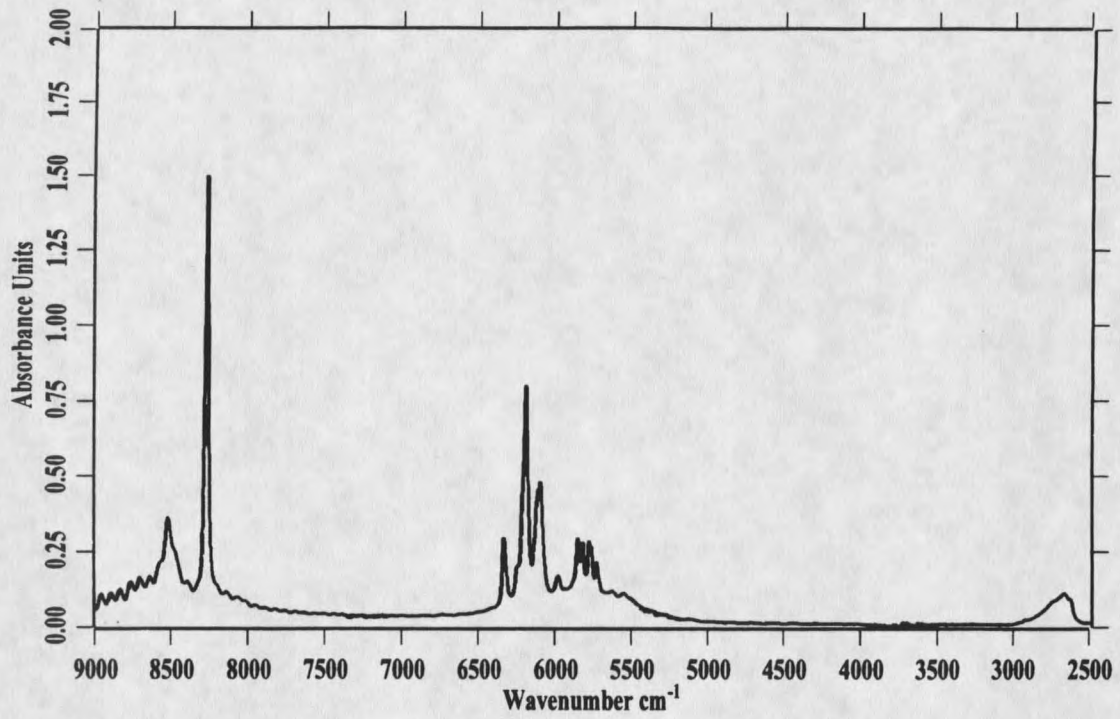


Figure 16. IR (top) and visible absorption spectra for Tm<sup>3+</sup>:YSO.

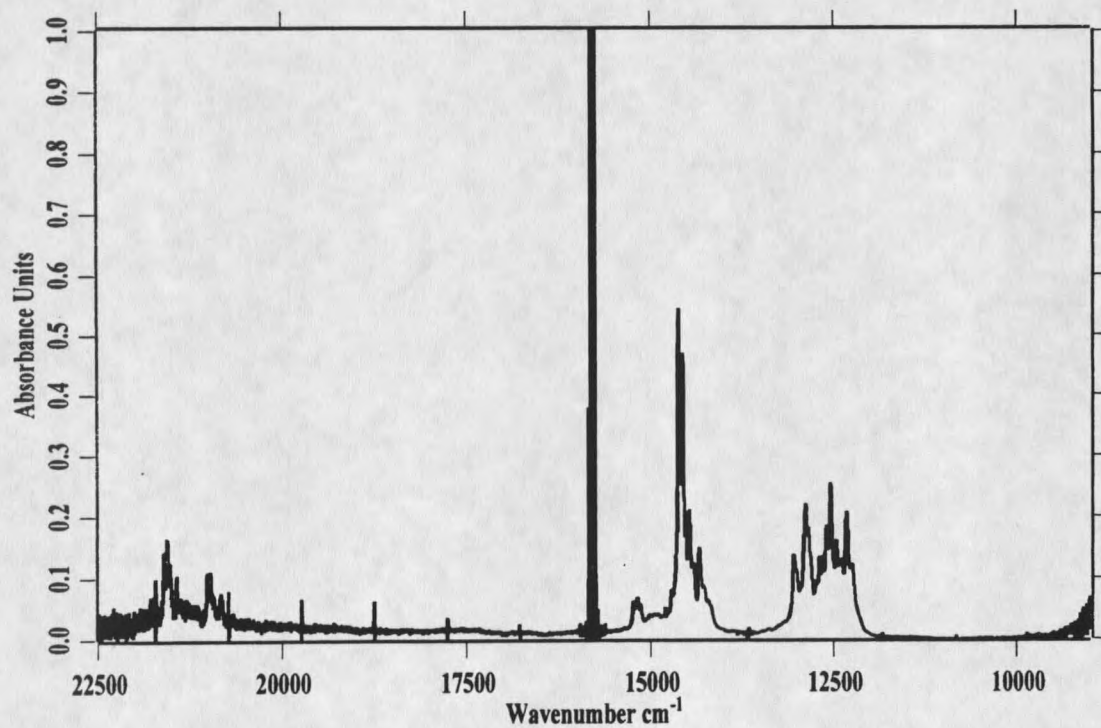
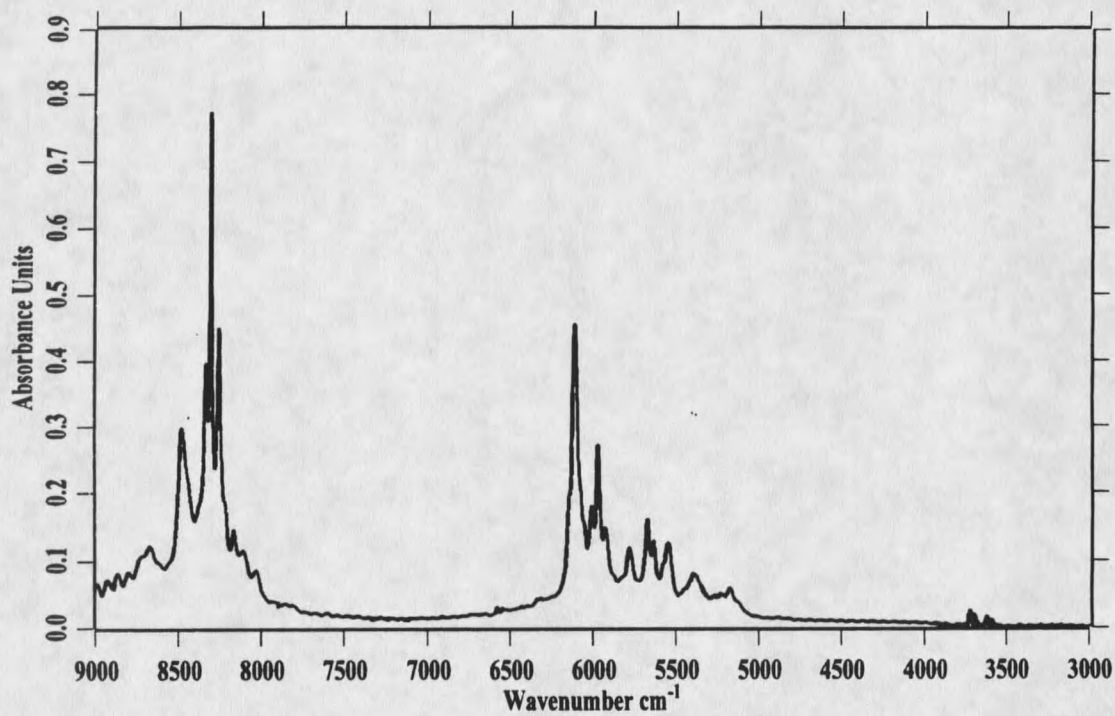


Figure 17. IR (top) and visible absorption spectra for  $\text{Tm}^{3+}:\text{YO}$ .

ground state manifold to excited state manifolds. Also, inhomogeneous line broadening due to small spatial deviations of the  $\text{Tm}^{3+}$  ion from site to site within the crystalline lattice may also contribute to spectral broadening(3,6). The absorption features near  $22,000 \text{ cm}^{-1}$  of the  $^1\text{G}_4$  manifold show diminished S/N compared to the remainder of the visible spectrum due to the aforementioned decrease of the instrument response. A larger number of scans may enhance the absorption features. Shifts in the maximum absorption values for each manifold vary approximately  $100$  to  $400 \text{ cm}^{-1}$  as the host lattice is varied. The sharp peak centered at  $15,798 \text{ cm}^{-1}$  in the visible spectra is the HeNe laser used for monitoring the moving mirror in the interferometer.

#### Continuous Fluorescence Spectra

Fluorescence spectra for various transitions at many temperatures for several  $\text{Tm}^{3+}$  doped laser materials have been presented previously(1,37,39,40,42,43). The data obtained in this study are in agreement with the literature.

$\text{Tm}^{3+}$  is most often excited continuously by pumping the  $^1\text{D}_2$  manifold ( $29,000 \text{ cm}^{-1}$ ), the  $^1\text{G}_4$  manifold ( $21,700 \text{ cm}^{-1}$ ) or the  $^3\text{H}_4$  manifold ( $12,800 \text{ cm}^{-1}$ ). A GaAlAs diode laser which operates continuously at approximately  $12,820 \text{ cm}^{-1}$  ( $780 \text{ nm}$ ) and provides nearly  $2\text{W}$  of continuous lasing power was used as the excitation source when observing IR emission. Off-resonance excitation of the  $^1\text{G}_4$  Stark manifold was accomplished through the use of the  $454 \text{ nm}$  line of a continuous Ar ion laser. Excitation at this wavelength allowed for the observation of visible fluorescence.

Continuous fluorescence spectra are typically resolved to  $16 \text{ cm}^{-1}$  and  $64$  to  $1024$

scans are performed for signal averaging. Filters were rarely needed because the scattered laser light was not intense enough to saturate the detector. All emission experiments were performed at room temperature. The samples were excited by pumping at the edge of the face and the resulting emission was collected from the nearest side of the sample to minimize self-absorption processes.

Figures 18 through 22 (pgs. 42-46) show the fluorescence spectra which exhibit transitions from the  $^1G_4$ ,  $^3H_4$  and the  $^3F_4$  manifolds to the  $^3H_6$  ground state and other manifolds of higher energy. The emission frequency on the x-axis is in units of  $\text{cm}^{-1}$  and the intensity units on the y-axis are arbitrary. The spectra have been corrected for variations in the instrument response over the entire spectrum. The tungsten filament used operates at a temperature of 3500 K. A blackbody calculation was performed and factored into the instrument response to eliminate the sources contribution to the response curve. The IR spectrum is presented prior to the visible spectrum for each sample. Again, only one set of spectra are shown for  $\text{Tm}^{3+}:\text{YAG}$ ,  $\text{YALO}$ ,  $\text{YSO}$  and  $\text{YO}$ .

Comparing the spectra,  $\text{Tm}^{3+}:\text{YALO}$ ,  $\text{Tm}^{3+}:\text{YSO}$  and  $\text{Tm}^{3+}:\text{YO}$  exhibit relatively broad band-shapes and unresolved line-shapes, especially in the IR region. The spectra for  $\text{Tm}^{3+}:\text{YAG}$  and  $\text{Tm}^{3+}:\text{LAG}$  exhibit a much sharper line-shape in both the IR and visible spectral regions, however, all of the emission spectra are thermally broadened to a certain extent. The additional sharp line features in the visible spectra are caused by interference from the power supply of the  $\text{Ar}^+$  source.

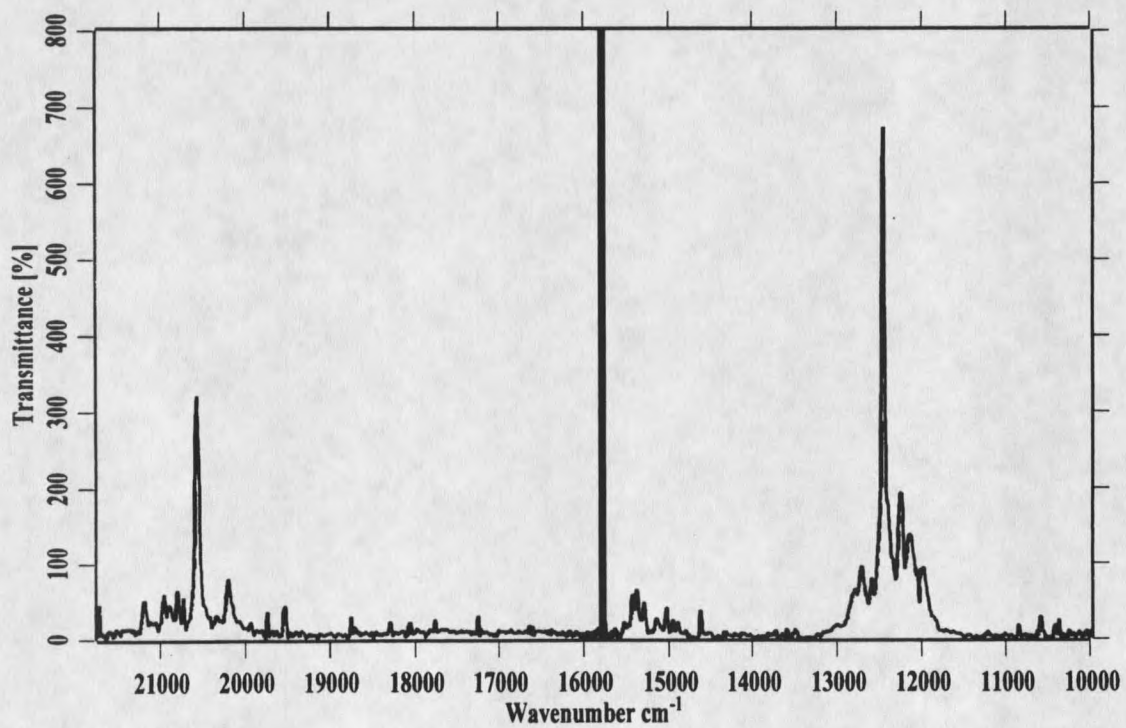
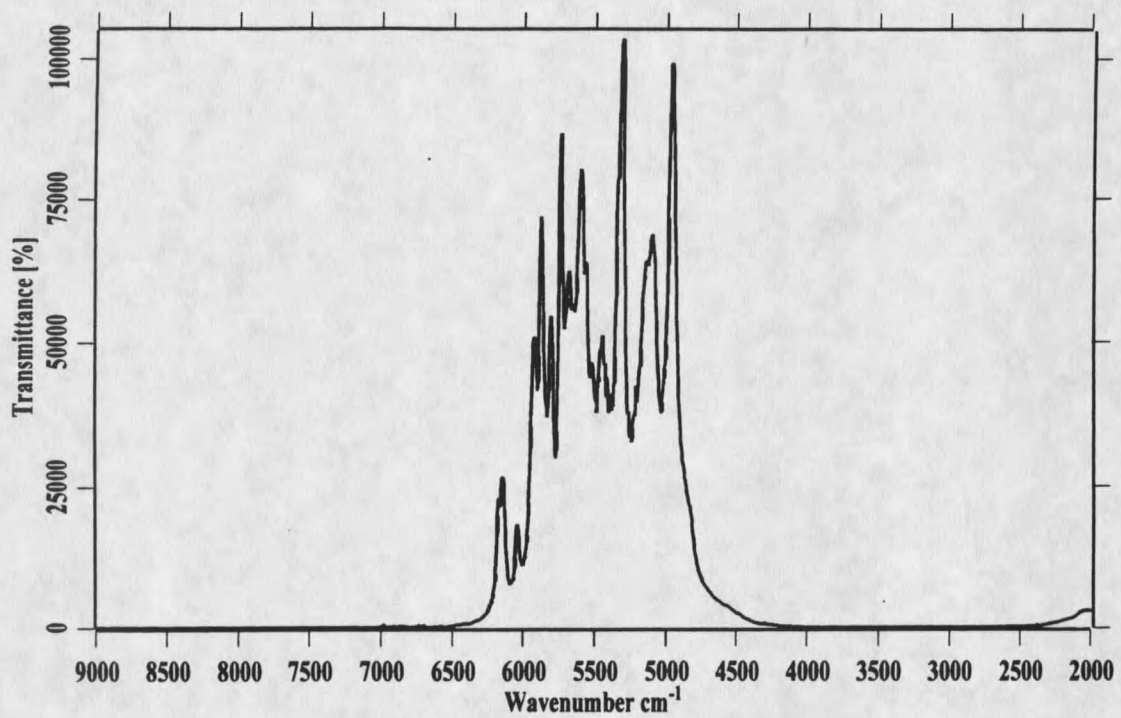


Figure 18. IR (top) and visible continuous emission spectra for Tm<sup>3+</sup>:YAG.

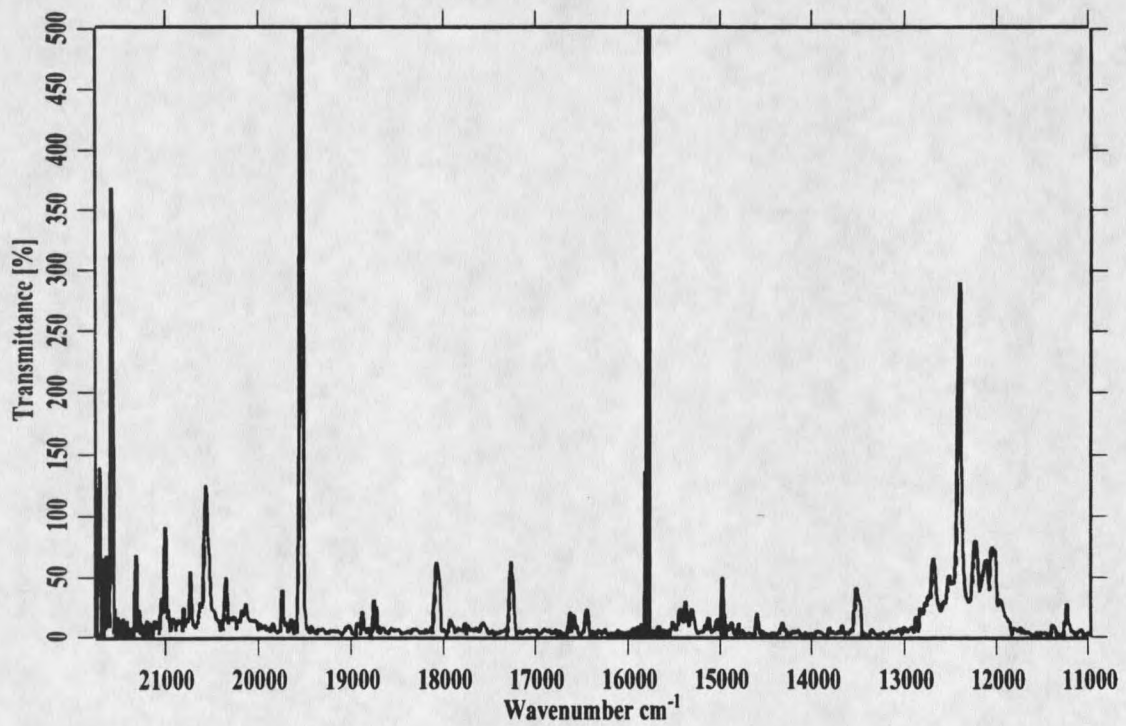
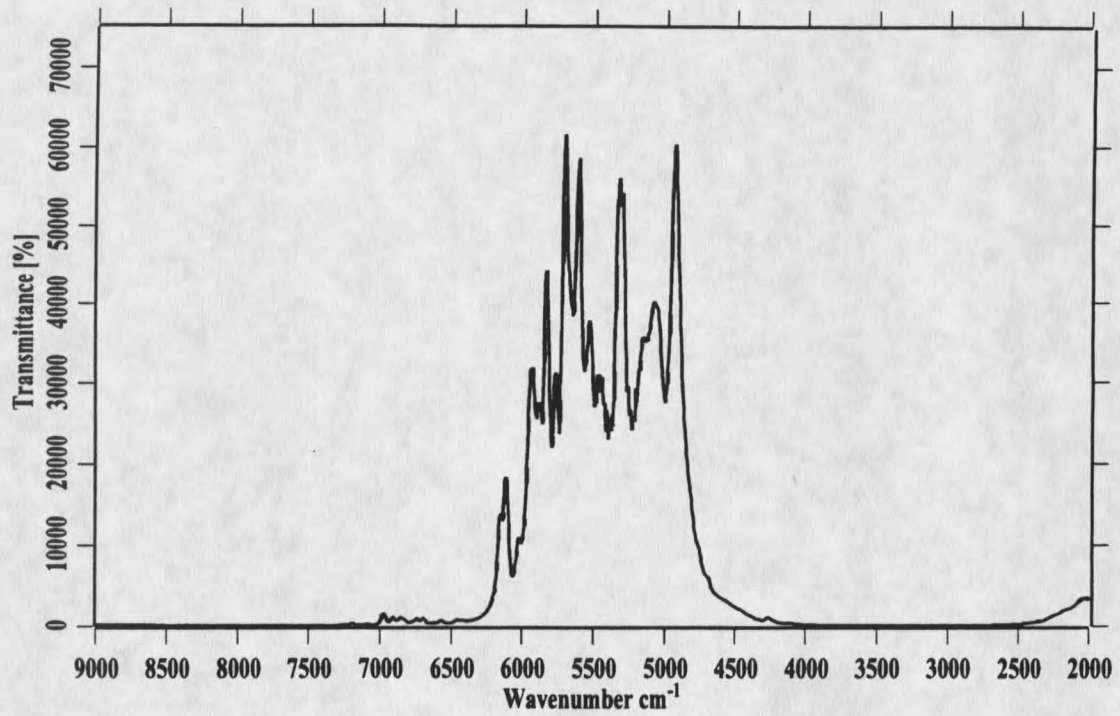


Figure 19. IR (top) and visible continuous emission spectra for  $\text{Tm}^{3+}:\text{LAG}$ .

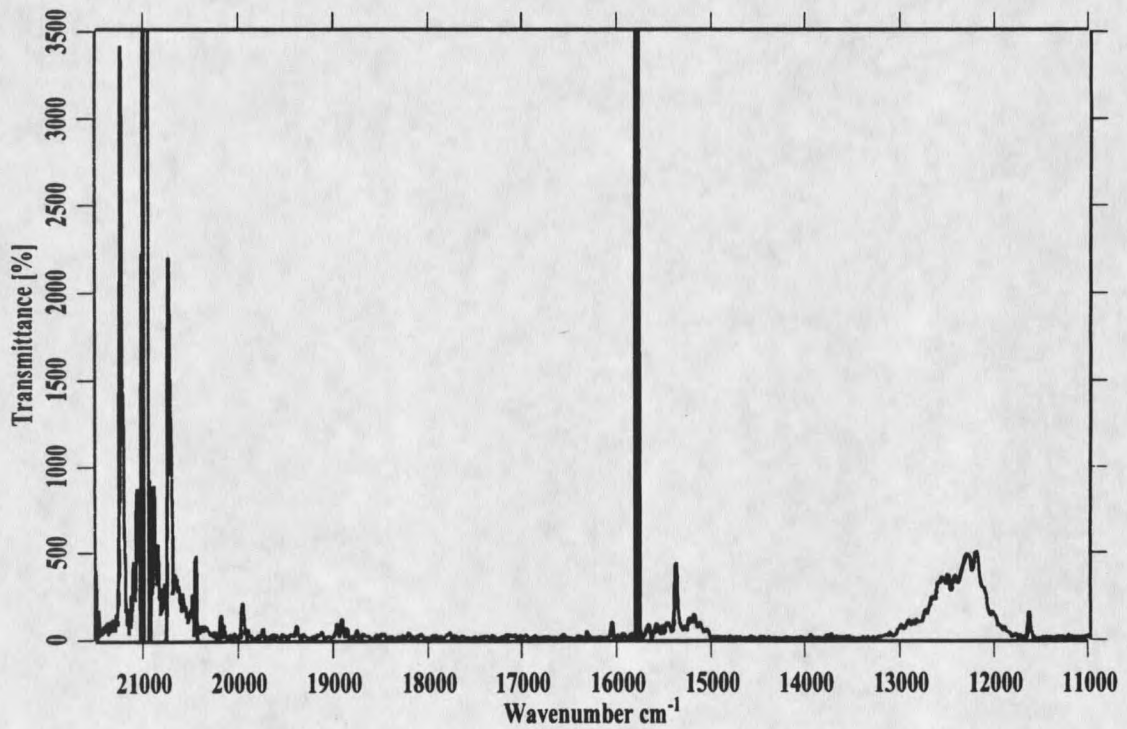
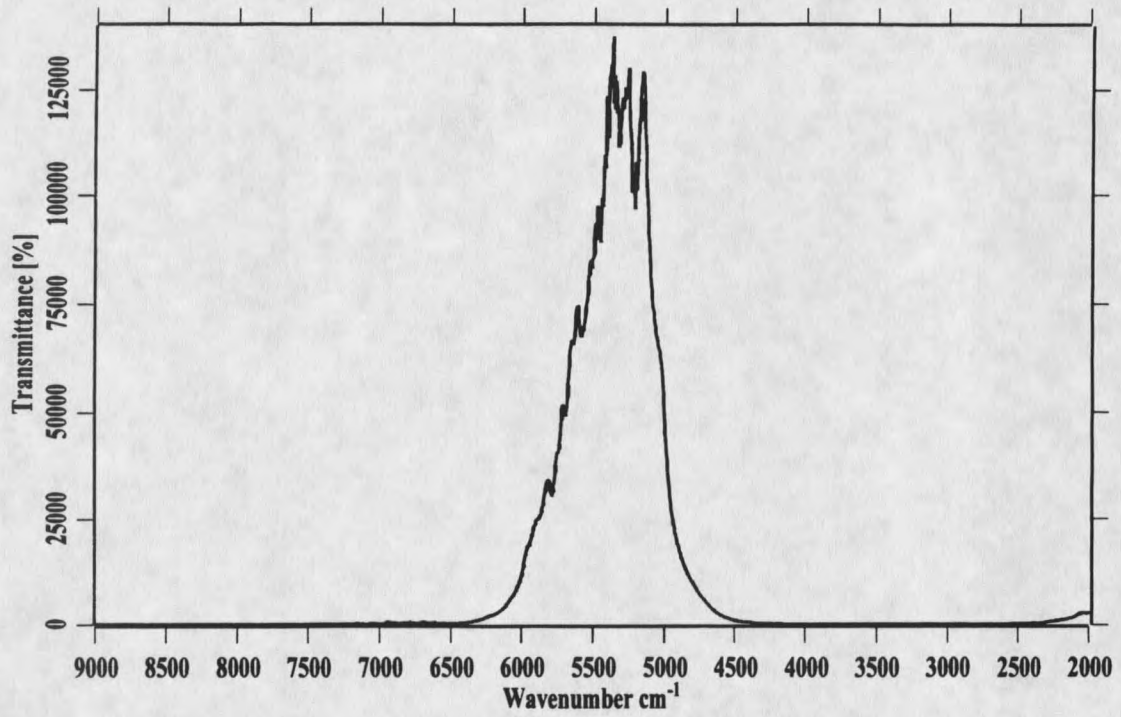


Figure 20. IR (top) and visible continuous emission spectra for  $\text{Tm}^{3+}:\text{YALO}$ .

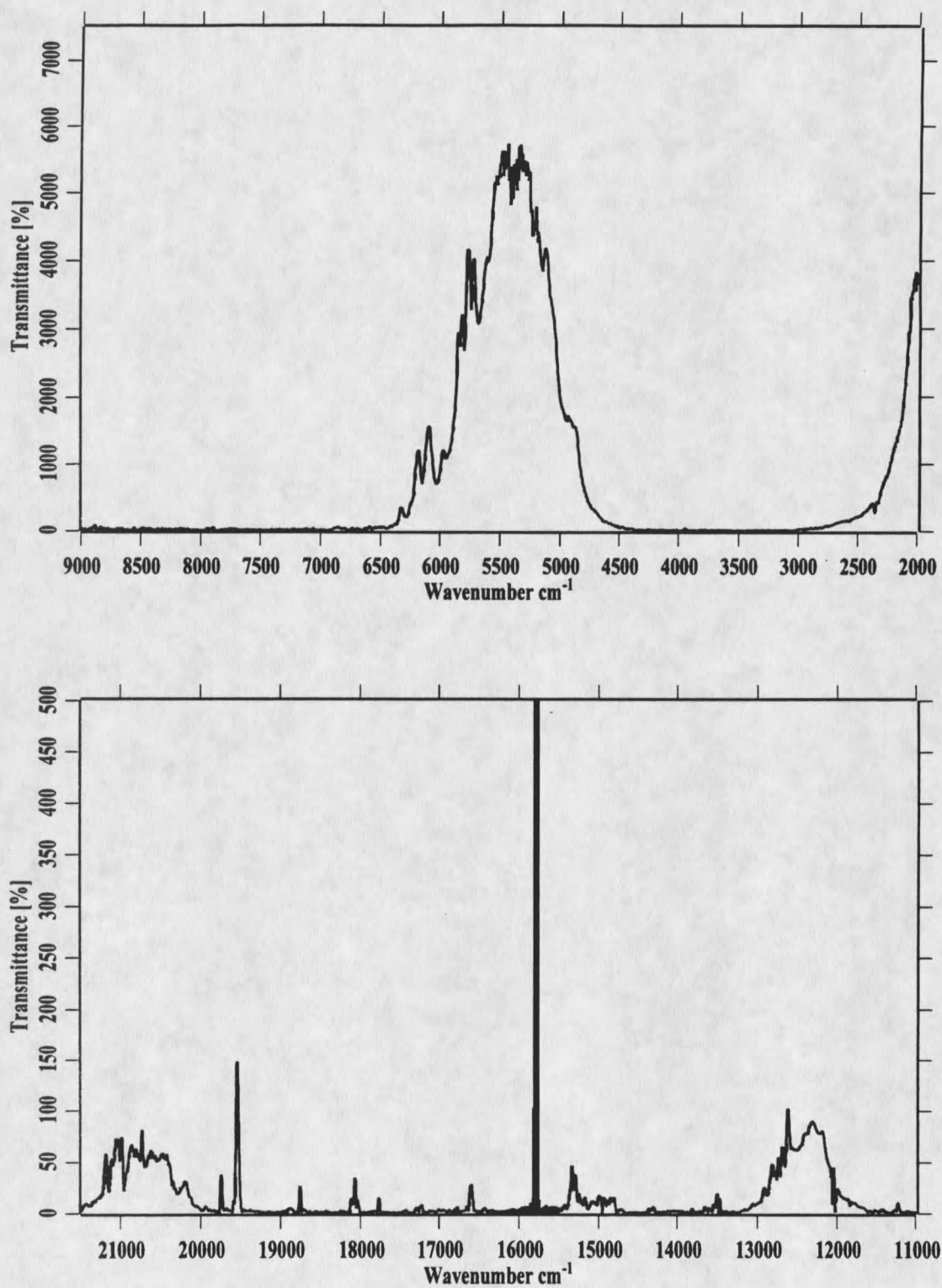


Figure 21. IR (top) and visible continuous emission spectra for  $\text{Tm}^{3+}:\text{YSO}$ .

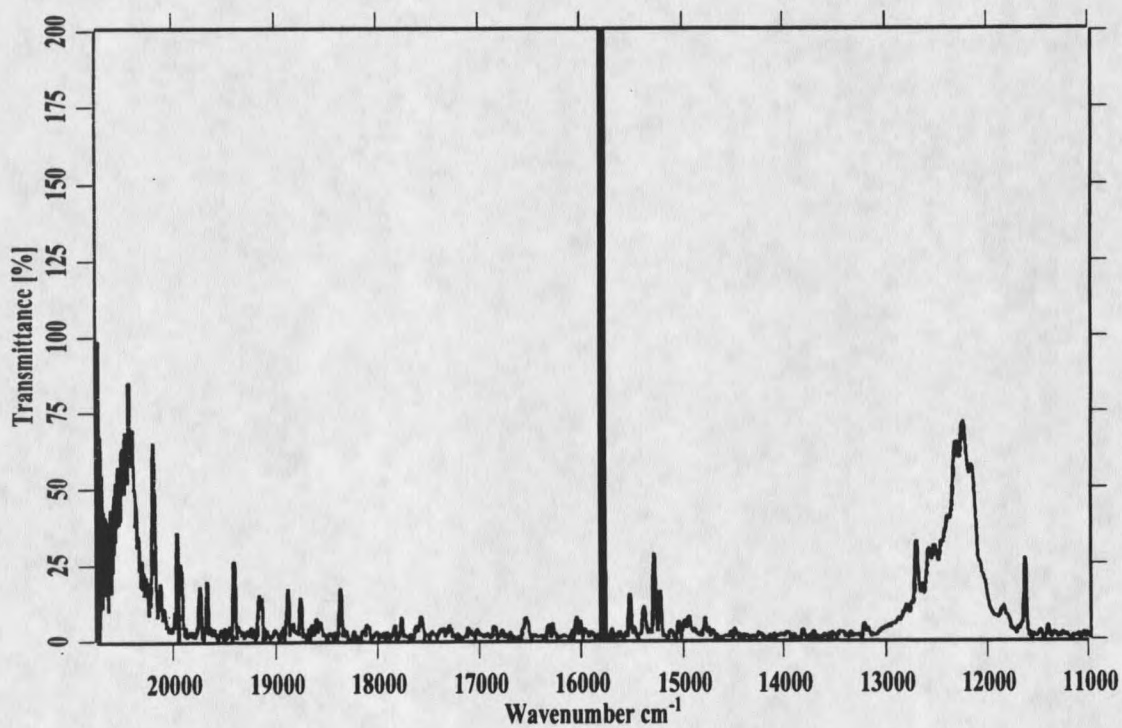
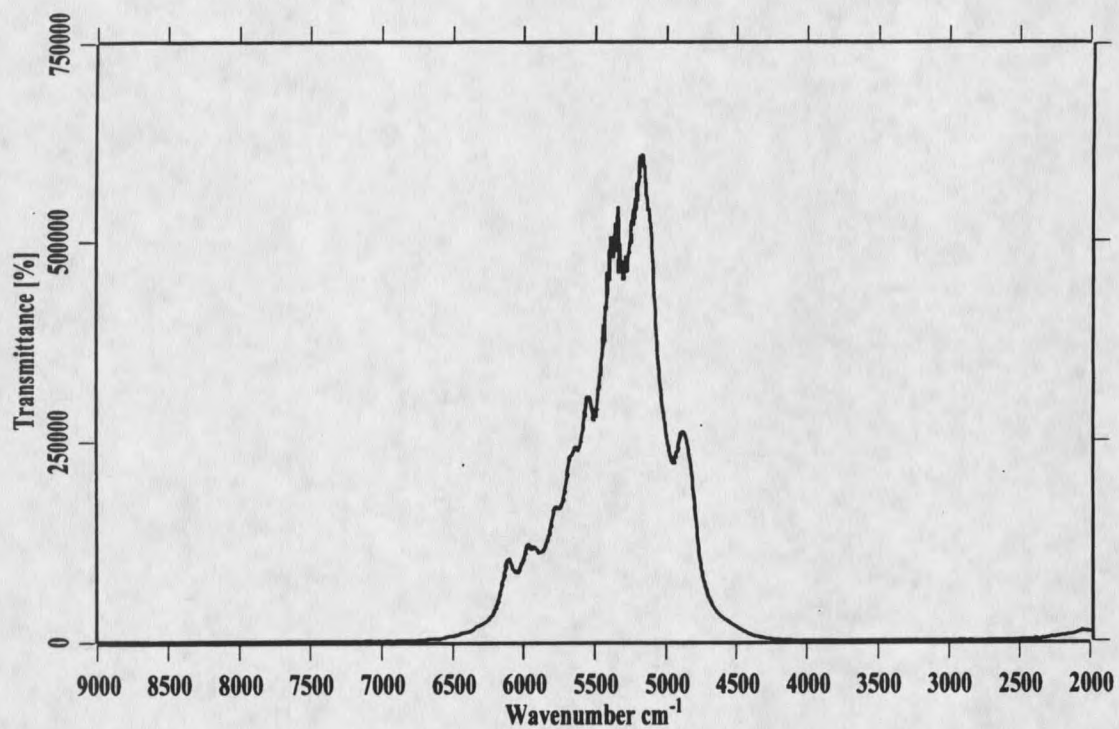


Figure 22. IR (top) and visible continuous emission spectra for  $\text{Tm}^{3+}:\text{YO}$ .

### Time-Resolved Fluorescence Spectra

The FT-TRS data is presented for each material or set of materials at every excitation wavelength used. In all plots, the x-axis is frequency in  $\text{cm}^{-1}$ , emission intensity is on the vertical y-axis and time (increasing from front to rear, unless noted) is on the z-axis. A brief summary of the experimental parameters will be given for each material due to subtle differences in data acquisition. The spectra have not been corrected for differences in the response curves for the visible and infrared spectral regions. Experimentally determined lifetimes are presented in Tables I and II at the conclusion of this chapter.

#### Excitation Via the $^3\text{H}_4$ Manifold

##### $\text{Tm}^{3+}:\text{YAG}$

Figure 23 shows the time-resolved fluorescence of the  $^3\text{F}_4 \rightarrow ^3\text{H}_6$  fundamental transition of 0.25 at. %  $\text{Tm}^{3+}:\text{YAG}$ . Each  $\text{Tm}^{3+}$  doped YAG sample was excited at  $12,800 \text{ cm}^{-1}$  (781.25 nm), using the idler OPO output, pumping the  $^3\text{H}_4$  manifold at either 10 or 15 Hz repetition rate. Idler output power for these experiments is on the order of 5 mJ/pulse. The interferometer was triggered on the positive edge of the TTL pulse from the Infinity system and no delays were used. Typically, for higher temporal resolution experiments ( $< 20 \mu\text{sec}$ ) the IFS 66 is triggered prior to the laser pulse to view one or two traces before excitation, however this is impractical for the longer experiments. The RG715 filter was used inside the OPO cavity to eliminate the signal wavelength and an Si filter was placed inside the interferometer to cut wavelengths

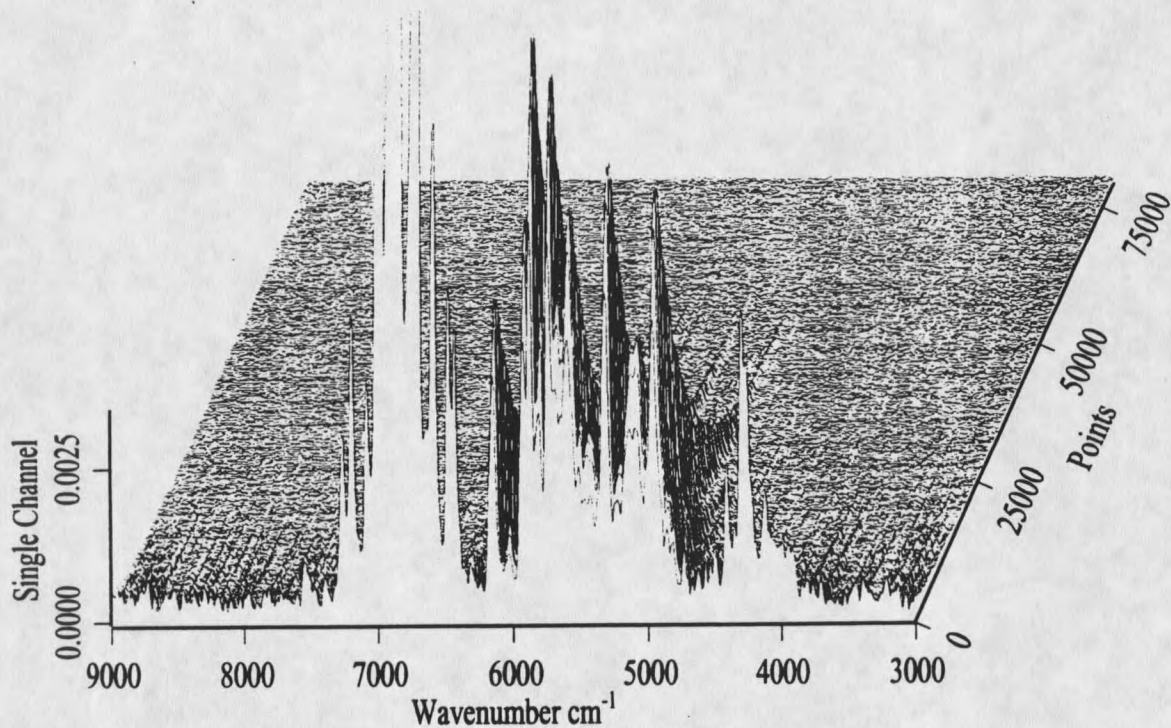


Figure 23. Time-resolved IR fluorescence spectrum for 0.25%  $\text{Tm}^{3+}:\text{YAG}$ . 400  $\mu\text{sec}$  time resolution, 200 time slices, 10 co-adds.

greater than  $9,000\text{ cm}^{-1}$  in energy when desired. The slower 16 bit recorder was used for these experiments and the wavelength region from  $9,000\text{-}2,000\text{ cm}^{-1}$  was studied. Temporal resolution for these experiments was  $500\ \mu\text{sec}$  with 200 time slices (sampling) and 10 co-additions (signal averaging) performed. This yields a total sampling time of 100 msec. Generally, a sampling time that is at least 4 to 5 times longer than the lifetime of the transition of interest is used. The  ${}^3\text{F}_4 \rightarrow {}^3\text{H}_6$  transition is known to be approximately 10-12 msec in duration(1,44,45) and, therefore a laser repetition rate of 20 Hz would be the maximum that would allow total relaxation to the ground state between pulses. The bandshape is relatively consistent between the 5 samples and

exhibits the well-known  $2\mu\text{m}$  transition, hence only one step-scan spectrum is shown for this process.

An integration of this transition over time yields a representative trace that appears to be purely exponential in behavior (see Figure 24). All trace plots are baseline

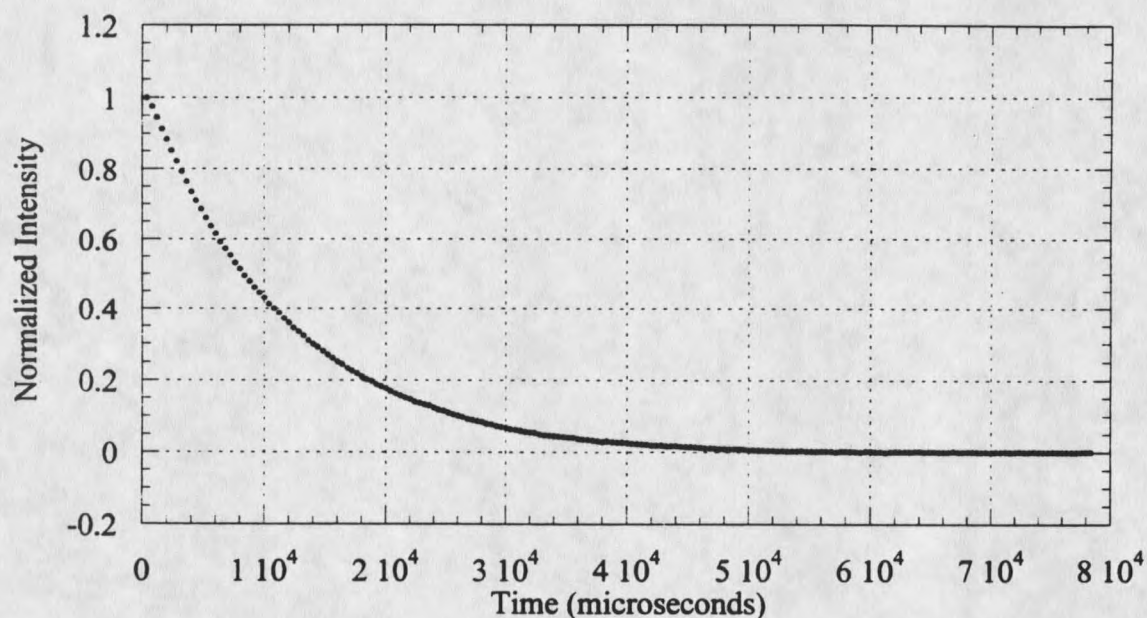


Figure 24. Decay of the  ${}^3\text{F}_4 \rightarrow {}^3\text{H}_6$  transition for the 0.25%  $\text{Tm}^{3+}:\text{YAG}$  sample.

corrected and normalized to a maximum intensity value of 1.0 for comparison between spectra.

The lifetime of the fundamental transition calculated from this data ranges from 11.21 to 11.79 msec with no observable dependence on the concentration of the dopant ion. Two additional bands centered at approximately  $6,800\text{ cm}^{-1}$  and  $4,300\text{ cm}^{-1}$  are readily observed and can be attributed to transitions originating from the  ${}^3\text{H}_4$  pump manifold. Increasing the time resolution was necessary to characterize the lifetimes of

these faster emission processes. Inspecting Figure 25, one can see four emission bands

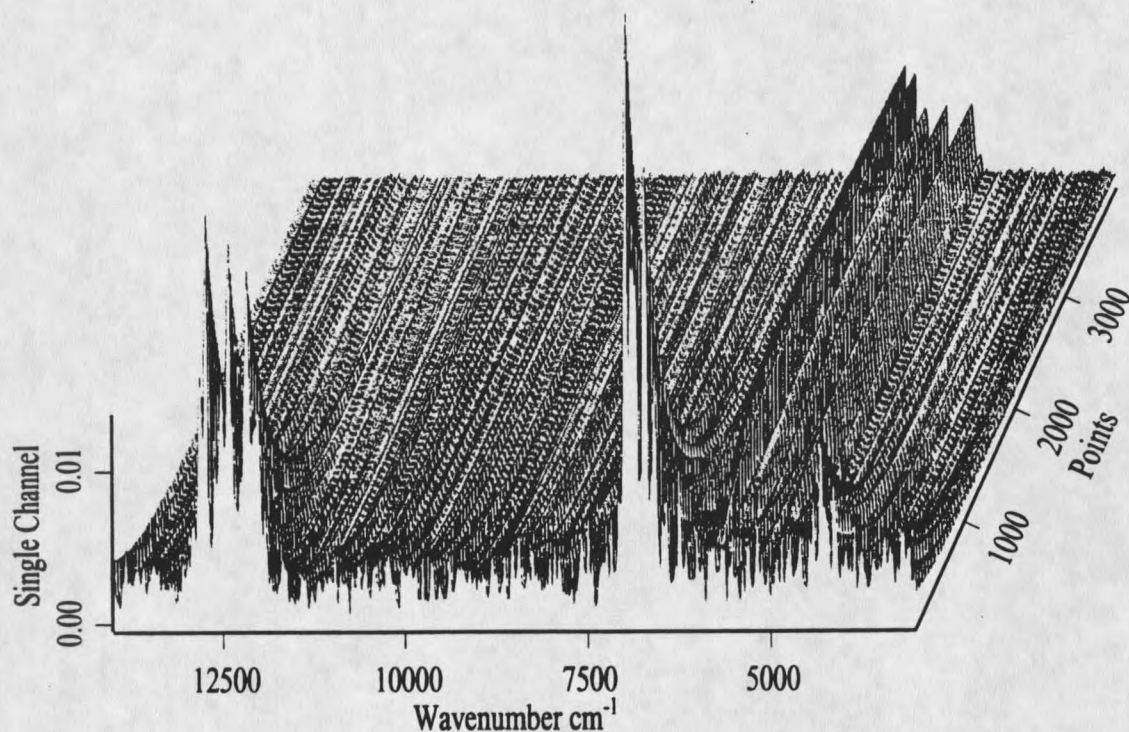


Figure 25. Time-resolved IR fluorescence spectrum for 0.25%  $\text{Tm}^{3+}$ :YAG. 20  $\mu\text{sec}$  time resolution, 200 time slices and 20 co-adds.

centered at 12,700, 6,800, 5,500 (rising) and 4,300  $\text{cm}^{-1}$ . Experimental conditions were similar to the longer time-based experiment except that a Si filter was not used and a wavelength range of 15,750 - 2,000  $\text{cm}^{-1}$  was studied. The 16 bit recorder was used for this experiment where the time resolution was 5 to 20  $\mu\text{sec}$  with 200 time slices and 20 coadditions (signal averaging) which yields 10 msec of total acquisition time. The faster 8 bit recorder was used for 5.25%  $\text{Tm}^{3+}$  where the temporal resolution was 1  $\mu\text{sec}$ .

The emission band centered at about 6,800  $\text{cm}^{-1}$  has been assigned to the  ${}^3\text{H}_4 \rightarrow {}^3\text{F}_4$  transition. The weak band centered at about 4,300  $\text{cm}^{-1}$  is the  ${}^3\text{H}_4 \rightarrow {}^3\text{H}_5$  transition. An additional band centered at around 12,700  $\text{cm}^{-1}$  is the  ${}^3\text{H}_4 \rightarrow {}^3\text{H}_6$  transition. This band





































































































